Master's thesis

NTNU
Norwegian University of Science and Technology
Faculty of Natural Sciences
Department of Materials Science and Engineering

Helene Lillevestre Langli

Side reactions on two types of carbon conductive additives in ionic liquid-based electrolytes for high voltage Li-ion battery cathodes

Master's thesis in Materials Science and Engineering
Supervisor: Ann Mari Svensson
Co-supervisor: Inger-Emma Nylund
June 2023

NTNU
Norwegian University of
Science and Technology

Helene Lillevestre Langli

Side reactions on two types of carbon conductive additives in ionic liquid-based electrolytes for high voltage Li-ion battery cathodes

Master's thesis in Materials Science and Engineering
Supervisor: Ann Mari Svensson
Co-supervisor: Inger-Emma Nylund
June 2023

Norwegian University of Science and Technology
Faculty of Natural Sciences
Department of Materials Science and Engineering

NTNU
Norwegian University of
Science and Technology

Preface

This thesis is the end of my master's degree and a result of the subject TMT4905 Materials Technology, Master's Thesis. The work was carried out at the Department of Materials Science and Engineering at the Norwegian University of Science and Technology. First, I would like to thank my supervisor Ann Mari Svensson for her invaluable guidance and feedback throughout the entire project. Second, I would like to express gratitude to my co-supervisor Inger-Emma Nylund for guidance in how to make cathodes and assemble cells, in addition to giving advice on the use of SEM and helping me mount samples for XRD analysis. She, together with my co-worker Mika Serna Malmer, mixed the electrolytes I used this semester, and I would like to thank them for that. Johan Hamonnet is thanked for giving great feedback and contributing to good discussions. Next, I would like to express gratitude to Camilla Lian for helping with the analysis of the XRD data, and for teaching me how to mount samples for FTIR. Further training on how to do FTIR was given by Johannes Ofstad, and I thank him for that. I would like to express gratitude to Elvia Anabela Chavez Panduro and Harald Norrud Pollen for their help and guidance with the XRD measurements, and Harald also mixed the PVDF solutions I used for this work. Then, I thank the battery group at NTNU for their valuable input. The Research Council of Norway is acknowledged for the support to the Norwegian Micro- and Nano-Fabrication Facility, NorFab, project number 295864.

During this work, I have collaborated with Mika Serna Malmer, who has also been writing a master's thesis this semester. The focus of his work has been on the degradation of the LNMO active material during cycling in conventional and ionic liquid electrolyte.

Abstract

Lithium-ion batteries (LIBs) are a good option for energy storage in electric vehicles, stationary storage, *e.g.* in relation to solar cells, and many other applications. Even though these batteries are highly commercialised, there is still much room for improvement, and less expensive batteries with better properties are wanted. The relatively low cost and high energy density, originating from its high operating voltage, makes $LiNi_{0.5}Mn_{1.5}O_4$ (LNMO) an interesting cathode material for future commercial batteries. However, the use of this material is also accompanied by issues. In this work, unwanted reactions at two types of carbon at high voltages are investigated, to understand the effect of the conductive carbon additive on reactions at high voltages. To do this, cathodes with only carbon black and binder and only graphite and binder were made, and cells with these and ionic liquid (IL)-based electrolytes underwent cyclic voltammetry between 3 V and 5 V. The two electrolytes were 0.79m and 3m lithium bis(fluorosulfonyl)imide (LiFSI) in the IL trimethyl(isobutyl)phosphonium bis(fluorosulfonyl)imide ($P_{111i4}FSI$). Based on the voltammograms and *post mortem* characterisation of the cathodes, a better understanding of the reactions is gained. Cells with an LNMO cathode with graphite as the conductive additive, together with 0.79m LiFSI in the IL as the electrolyte, were also made and exposed to galvanostatic cycling.

It is found that the graphite cathodes suffer from anion intercalation in addition to electrolyte degradation at the surface. The carbon black cathodes virtually only experience surface reactions. It is further decided that the anion intercalation degrades the graphite structure, which causes increased electrolyte oxidation. The electrolyte oxidation creates a film shown to consist of sulfur and oxygen, though fluorine and nitrogen, also originating from the anion, can be present. The film at the graphite cathodes is different from that at the carbon black cathodes, but they are made of the same chemical species, and the exact differences are unknown. Similar trends are observed with the two different electrolytes, but using 3m LiFSI instead of 0.79m LiFSI reduces the amount of anion intercalation, and causes precipitation of LiFSI salt. Combining

graphite as the conductive additive of an LNMO cathode and 0.79m LiFSI in the IL as the electrolyte causes a poor discharge capacity due to a poor electronic conductive network. The efficiency is comparable to the reference cell. Anion intercalation into graphite occurred, and there was also a film formation which happened more at the graphite than LNMO.

Sammendrag

Litium-ionbatterier (LIBs) er et godt alternativ for energilagring i elektriske kjøretøy og stasjonær lagring, for eksempel sammen med solceller, i tillegg til å ha mange andre bruksområder. Selv om disse batteriene allerede er kommersielt tilgjengelige, er det mye som kan forbedres, og man ønsker billigere batterier med bedre egenskaper. $LiNi_{0.5}Mn_{1.5}O_4$ (LNMO) sin relativt lave pris og høye energitetthet, som kommer fra den høye spenningen det oppererer på, gjør at det forskes på for bruk som katode-materiale i fremtidige kommersielle batterier, men det er flere problemer knyttet til materialet. I dette arbeidet undersøkes uønskede reaksjoner på to typer karbon for å forstå hvilken effekt det elektrisk ledende karbon additivet har på reaksjoner ved høye spenninger. Dette gjøres ved at det blir lagd katoder kun bestående av "carbon black" og bindemiddel, og katoder med kun grafitt of bindemiddel. Disse katodene ble brukt i celler sammen med enten 0.79m lithium bis(fluorosulfonyl)imide (LiFSI) i trimethyl(isobutyl)phosphonium bis(fluorosulfonyl)imide ($P_{111i4}FSI$) eller 3m LiFSI i $P_{111i4}FSI$ som elektrolytt, og de gjennomgikk deretter syklisk voltammetri mellom 3 V og 5 V. Basert på voltammogrammene og videre karakterisering av katodene har man fått en bedre forståelse for reaksjonene. Det ble også gjennomført galvanostatisk sykling av celler med LNMO som aktivt katode-materiale, grafitt som elektrisk ledende additiv i katoden og elektrolytten med 0.79m LiFSI i $P_{111i4}FSI$.

Det er tydelig at grafittkatoder utsettes for anioninterkalasjon i tillegg til elektrolyttdegraderingen som skjer på overflaten. "Carbon black"-katodene utsettes omtrent bare for overflatereaksjoner. Det er videre bevist at anioninterkalasjonen degraderer grafittstrukturen, og at de degraderte partiklene skaper mer elektrolyttoksidasion. Elektrolyttdegraderingen skaper en overflatefilm bestående av svovel og oksygen, i tillegg til at nitrogen og fluor, også fra anionet, kan være en del av den, selv om dette ikke kunne bevises. Det er videre funnet at den kjemiske komposisjonen på overflaten er ulik for syklede grafittkatodene og "carbon black"-katodene, men de samme kjemiske komponenetene er tilstede, og den eksakte forskjellen er ukjent. Man ser samme trend for reaksjonene ved bruk av de to ulike elektrolyttene, men noen forskjeller er også

oppdaget. Bruk av elektrolytten med 3m LiFSI fører til det blir mindre anioninterkalasjon, men det ble oppdaget utfelling av LiFSI-salt etter syklingen. Cellene med LNMO og grafitt i katoden, samt elektrolytten med 0.79m LiFSI, har dårlig utladningskapasitet fordi det elektrisk ledende netverket er dårlig. Effektiviteten var derimot tilnærmet lik referansecellen. Både anioninterkalasjon og film-dannelse ble oppdaget, og det ble dannet mer film på grafitten enn LNMO-partiklene.

Abbreviations

ATR	Attenuated total reflectance
CEI	Cathode-electrolyte interphase
CMC	Carboxymethyl cellulose
CV	Cyclic voltammetry
DEC	Diethyl carbonate
DMC	Dimethyl carbonate
EC	Ethylene carbonate
EDS	Energy dispersive X-ray spectroscopy
FTIR	Fourier transform infrared spectroscopy
GCPL	Galvanostatic cycling with potential limitation
LCO	$LiCoO_2$
LFP	$LiFePO_4$
LIB	Lithium ion battery
LiFSI	Lithium bis(fluorosulfonyl)imide
$LiPF_6$	Lithium hexafluorophosphate
LNMO	$LiNi_{0.5}Mn_{1.5}O_4$
NMC	$LiNi_xCo_yMn_zO_2$
NMP	N-methyl-2-pyrrolidone
$P_{111i4}FSI$	Trimethyl(isobutyl)phosphonium bis(fluorosulfonyl)imide
PVDF	Polyvinylidene fluoride
SEI	Solid-electrolyte interphase
SEM	Scanning electron microscopy
XPS	X-ray photoelectron spectroscopy
XRD	X-ray diffraction

Contents

Chapter 1

Introduction

Development towards increased use of alternative energy sources, like wind and solar power, is part of the change towards a more sustainable future. However, this development is also accompanied by problems. Indeed, as both wind and solar powers depend on the weather, it is essential to develop suitable methods of energy storage [1][2], so that the stored electricity is accessible when needed. The increasing popularity of electric vehicles also reinforces the need for quality energy storage [3]. These are two of many applications where lithium-ion batteries (LIBs) are good options for the energy storage, as they combine high power density with high energy density [4]. LIBs are already used in a wide variety of commercial applications, such as small-scale portable devices like laptops and cell phones and electric vehicles [5]. Considering that LIBs are thought to be the dominating battery technology for the coming decade and possibly for much longer [6], continuous research and improvement of the technology is required. Even though LIBs have been researched for decades, there is still much room for improvement, and batteries with longer lifetimes, higher capacities and better rate capabilities are wanted. In order to improve the technology, the cell components and their mutual interactions must be considered [7].

Multiple types of cathode active materials are used in today's commercialised batteries, but none are flawless. The search for a better cathode material has led to extensive research into $LiNi_{0.5}Mn_{1.5}O_4$ (LNMO). It is a cathode material free of Co, which is expensive, toxic, has a low abundance in the earth's crust, and is also mined by children [8][9]. LNMO also has a high energy density and good thermal stability [8][10]. Still, some issues must be solved before the commercialisation of LNMO cathodes. One is the unwanted side reactions with the electrolyte taking place because of the high operating voltage [8]. All cathodes use conductive carbon additives, as the active

materials have low electronic conductivity, insufficient for the electrodes. This carbon typically has a much larger surface area than the active material, so it can be assumed that this material plays a critical role in the electrolyte oxidations [11][12]. Ionic liquids (IL)-based electrolytes have also gained more attention lately, due to their superior thermal stability, large electrochemical windows, and other advantages over commercial carbonate-based electrolytes.

The main aim of the work is to study the side reactions on two different carbon conductive additives in an IL-based electrolyte at high voltages, up to 5 V *vs.* Li/Li^+. One graphitic conductive additive, and one carbon black conductive additive was compared, and based on a combination of electrochemical techniques and *post mortem* studies, the reversibility of the side reactions and composition of films formed could be identified.

This investigation was conducted by making cathodes consisting of only the carbon material with a binder, to eliminate the effects of LNMO on the side reactions. Half cells with these cathodes and two different IL-based electrolytes were made, and cyclic voltammetry was done to identify possible side reactions. *Post mortem* characterisation in this work was scanning electron microscopy (SEM), Energy dispersive X-ray spectroscopy (EDS), Fourier transform infrared spectroscopy (FTIR) and X-ray diffraction analysis (XRD). Following this first work, LNMO cathodes with graphite as conductive carbon were made and incorporated into half cells with one of the IL-based electrolytes. These were compared to a reference cell through galvanostatic cycling and SEM imaging, together with EDS.

Chapter 2

Theory

2.1 An overview of lithium-ion batteries

In LIBs, Li^+ ions move through the electrolyte between the two electrodes. In this section, the fundamentals of LIBs will be discussed, and if nothing else is given, the source used is the book *Lithium Batteries: Science and Technology* by Julien, Mauger, Vijh and Zaghib [7].

2.1.1 Working principles

A LIB has a positive and a negative electrode and an electrolyte between these. The electrodes are also connected by an outer circuit. Figure 2.1 shows a schematic figure of a LIB. Upon discharge, the positive electrode is the cathode, and the negative electrode is the anode. When discussing batteries, it is common to refer to the positive electrode as the cathode, even during charging. The negative electrode is then referred to as the anode. This way, when talking about cathode materials, it is understood that this is the material at the positive electrode and that the anode materials are at the negative electrode. Graphite is commonly used as the anode material in commercial batteries due to the abundance of carbon, and its good cycling stability [13]. Different cathode materials are utilised today, and some will be further described in section 2.3. The electrode materials are cast onto current collectors, which ensures the transport of electrons from the electrodes to the outer circuit. Aluminium is commonly used as the current collector on the cathode side, while copper is widely used on the anode side. Organic solvents with appropriate Li salts are usually used as electrolytes in the LIBs, and the Li^+ ions move through the electrolyte from one electrode to the other.

There is also a separator between the two electrodes, which inhibits physical contact between the electrodes, preventing short circuits. Separators are commonly made of polymers like polyethylene and polypropylene.

The battery reactions happening will depend on the electrode materials. If the anode is made of graphite, and the cathode of $LiCoO_2$ (LCO), the following electrochemical reaction will happen at the cathode:

$$LiCoO_2 \rightleftharpoons Li_{1-x}CoO_2 + xLi^+ + xe^- \tag{2.1}$$

At the anode, the electrochemical reaction will be:

$$xLi^+ + xe^- + 6C \rightleftharpoons Li_xC_6. \tag{2.2}$$

In both equations, the top arrows are the reactions occurring during charge, while the bottom arrows are the reactions during discharge. From this, the total cell reaction is

$$LiCoO_2 + 6C \rightleftharpoons Li_{1-x}CoO_2 + Li_xC_6. \tag{2.3}$$

The Li^+ ions arriving at an electrode are intercalated into the electrode materials. In other words, the ions go into the material's structure and become a part of it. For the graphite, they go in between the layers of the carbon structure. For LCO the Li^+ ions are also found in the layers, more specifically, between planes made up of oxygen molecules. It should also be noted that alloying reactions, where lithium creates an alloy with the electrode material [14], and conversion reactions, where chemical bonds are broken and formed during charge and discharge [15], are alternatives to the intercalation reactions in LIBs.

2.1.2 Terminology and important parameters

There are many criteria a battery must fulfil depending on its intended use. The critical parameters for batteries will be discussed in the following subsection.

The Open circuit voltage V_{oc} is given as

$$V_{oc} = -\frac{1}{nF}(\mu_A^i - \mu_C^i) \tag{2.4}$$

where n is the moles of electronic charge taking part in the reaction, F is Faraday's constant, and μ_A^i and μ_C^i are the electrochemical potentials of the anode and the

cathode, respectively. This value is the voltage when no current is flowing, and it limits the operating voltages of the cell.

Output and input voltage are the operating voltages of the cell during discharge and charge, respectively. The output voltage V_{dis} is lower than the open circuit voltage, while the input voltage V_{ch} will be higher than the open circuit voltage. This is caused by the battery's internal resistance [16].

Resistances in a battery are crucial for performance. The internal battery resistance R_b is

$$R_b = R_{el} + R_{in}(A) + R_{in}(C) + R_C(A) + R_C(C) \tag{2.5}$$

where (A) and (C) stand for anode and cathode. R_{el} is the electrolyte resistance, R_{in} is the resistance related to ionic transport across the electrolyte-electrode interface, and R_C is the intrinsic resistance of the electrodes.

The energy E, which can be obtained from a fully charged battery, depends on the charge q and the potential V during the transport of charge between the electrodes.

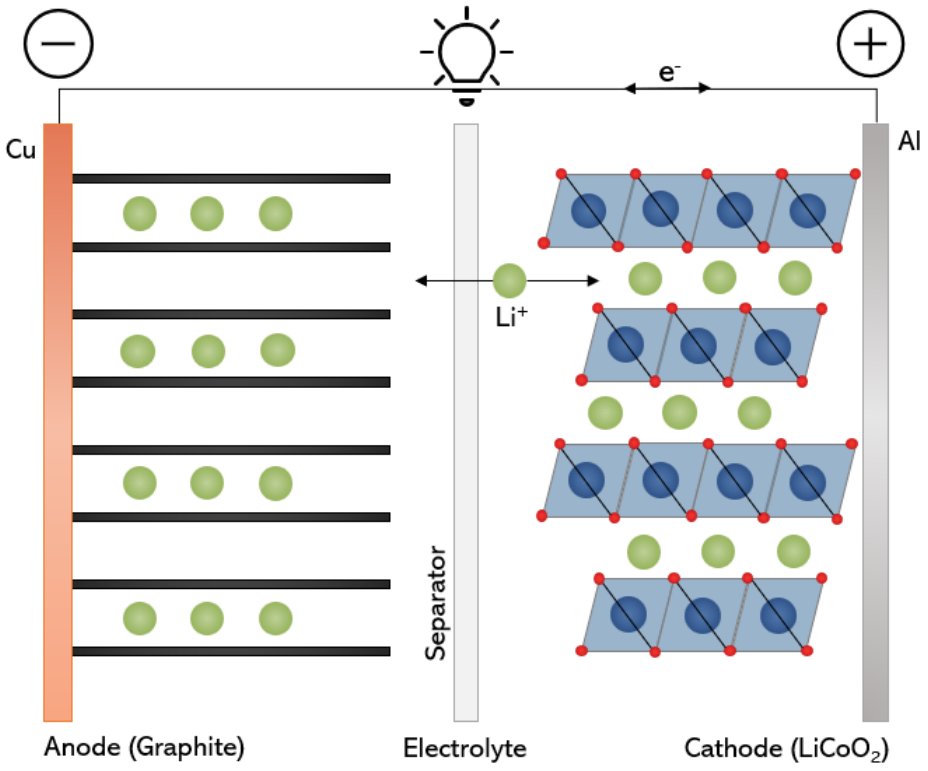

Figure 2.1: Schematic image of the components of a LIB, here visualised with graphite at the anode and LCO as the cathode material.

The equation

$$E = \int_0^Q V(q)dq \tag{2.6}$$

can be used to calculate the value, given that the current is kept constant during the discharge [16]. For batteries, the gravimetric and the volumetric energy densities are of high importance. These values are the amount of energy that can be stored per weight and per volume of the battery, respectively.

The Specific capacity Q_{th} (Ah/kg) is the amount of charge that can be stored in the electrode per weight and can be calculated with the equation:

$$Q_{th} = \frac{1000nF}{3600M_w}. \tag{2.7}$$

M_w is the molecular mass of the electrode material. This equation only provides the specific capacity for the electrode materials, and the battery capacity will be limited by the electrode material that can accommodate the lowest amount of lithium ions. When the goal is to create batteries with high capacities and low weight, the weight of the other battery components must also be considered. They do not increase the capacity but contribute to the total weight.

Coulombic efficiency CE measures how much the battery capacity fades in a charge/ discharge cycle. It is described by the equation:

$$CE(\%) = \frac{Q_{discharge}}{Q_{charge}} \cdot 100\%. \tag{2.8}$$

Irreversible capacity loss ICL can be described by the equation:

$$ICL = 1 - CE. \tag{2.9}$$

It is caused by volume changes, chemical reactions between electrolyte and electrode, and electrode decomposition. This causes the resistance in the battery to increase [16].

The *C*-rate normalises the charge or discharge current against the battery capacity. It is the rate at which the battery will be fully charged or discharged, relative to its maximum capacity. A rate of nC means the battery will be fully charged or discharged in $1/n$ hours.

The Cycle life of a battery is the number of charge/discharge cycles it can go through before the capacity is reduced to 80% of the original capacity.

The Shelf life is how long the battery can be stored before its capacity has been reduced so much that it is no longer appropriate for its intended use. Again, this is usually set to 80% of the original capacity [17].

2.2 The electrolyte

2.2.1 Properties of the electrolyte

In the ideal case, there are specific criteria that the electrolyte should fulfil. First, it should be stable against the electrodes to inhibit decomposition. Figure 2.2 shows the energy diagram for anode, electrolyte and cathode systems. The situation is stable if the Fermi energy levels E_C and E_A of the cathode and anode materials are within the energy gap E_g of the electrolyte. If the Fermi energies are outside the energy gap, unwanted reactions will happen, and the system will be unstable. To have ideal relations between E_g, E_C and E_A and at the same time have a high open circuit voltage, the energy gap of the electrolyte must be large, allowing for a larger potential difference between the cathode and anode materials [7]. A suitable electrolyte must also have high ionic conductivity, allowing fast transport of Li^+ ions and, therefore, a high rate of energy release. It must also have low electronic conductivity so that the self-discharge can be kept to a minimum [18]. It is also essential to have phase stability over an extensive range of temperatures to avoid evaporation or crystallisation of the liquid [7]. The other properties the electrolyte should exhibit are good wetting at the electrolyte-electrode interface, robustness against thermal, mechanical and electrical stress, and inertness towards all cell components. Sustainability is also of great importance, meaning that the electrolyte components used should be environmentally friendly, the raw materials should be abundant, and they should also be non-toxic and non-flammable.

2.2.2 Conventional electrolytes: Organic liquids and lithium salts

As previously discussed, today's conventional electrolytes are organic solvents with dissolved Li salts. The solvents should have a high boiling point and a low melting point, keeping them liquid at a large temperature range, and ensuring that the electrolyte functions properly. Low viscosity is also wanted, ensuring that the ions can

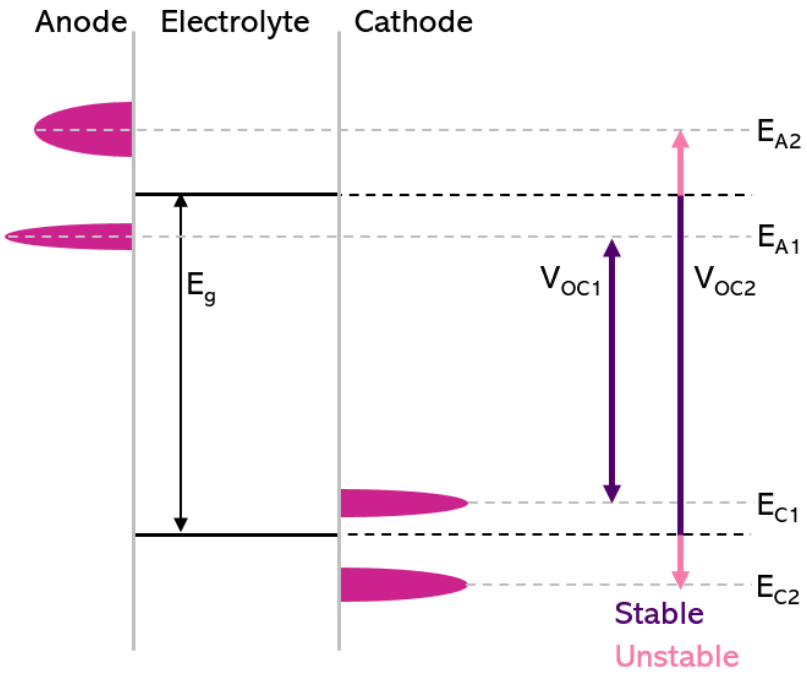

Figure 2.2: The energy diagram of a LIB. Two different situations are illustrated. In situation 1, the Fermi energy levels E_C and E_A are within the energy gap E_g of the electrolyte, and stability is ensured. Situation 2 has both E_C and E_A outside E_g, and instability at both electrodes will cause the electrolyte to degrade. Inspired by [7].

move easily. Another desired property is a large dielectric constant, which is beneficial for dissolving large solute concentrations. In addition, the solvent must be inert towards the cell components [18]. The Li salts should be fully dissociated at reasonably high concentrations. It should also be non-toxic, stable against overheating, and stable against reactions, meaning that the anions should not be oxidised at the cathode and inert to the solvent and the other electrolyte components [18].

Since the anodes in LIBs are strongly reductive, and the cathodes are strongly oxidising, solvents with active protons cannot be used. The anion oxidation and proton reduction often happen between 2.0 and 4.0 V *vs.* Li/Li^+. In comparison, the charged potentials of the anodes is usually are around 0 V, and the charged potential of the cathodes is generally between 3.0 and 4.5 V. The anion will then be oxidised at the cathode, and the proton will be reduced at the anode. To avoid this problem but still be able to dissolve sufficient amounts of Li salt, nonaqueous compounds with polar groups, such as carbonyl, nitrile, sulfonyl and ether linkage, are used as solvents for LIBs [18].

Many polar solvents have been investigated, most of which are either organic esters or ethers. Some commonly used solvents are ethylene carbonate (EC), dimethyl carbonate (DMC) and diethyl carbonate (DEC). DMC and DEC are linear carbonates,

while EC is a cyclic molecule. While DMC and DEC have similar dielectric constants of 3.1 and 2.8, respectively, the dielectric constant of EC is 89.8. This means that EC dissolves the Li salts more easily than the other solvents. This dependence of the dielectric constant on the molecular shape is also observed for other possible solvents. The cyclic esters have high dielectric constants, while those of the linear molecules are usually low. The viscosity is also highly dependent on the molecular shape of the esters. The linear ones, like DMC and DEC, have a low viscosity, while the cyclic ones have a high viscosity. The viscosities are 0.59 cP for DMC at 20°C, 0.75 cP for DEC at 25°C and 1.90 cP at 40°C for EC. To get a proper electrolyte, the dielectric constant of EC is wanted, but its high viscosity and melting point, which is at 36.4°C, makes it unsuitable at ambient temperatures. A common solution for this issue is to use a combination of EC and a linear carbonate. A sufficient amount of salt can then be dissolved while the viscosity is kept low enough that adequate ionic transportation is obtained [18].

The solute used in the electrolyte should fulfil certain criteria. First, it should be fully dissociated at relatively high concentrations, and second, it should have a high mobility of the Li^+ cation. This ensures good ionic conductivity. It is also preferred that it is non-toxic, thermally stable and has a low sensitivity to hydrolysis [7][19]. Lastly, the ions should be stable against reactions, which means that the anion should be inert to the solvent, stable against oxidation at the cathode, and both ions should be inert towards the other cell components [7]. A couple of wanted reactions are the initial formation of a solid-electrolyte interphase (SEI) layer at the anode, mitigating more unwanted reactions, and the formation of a protective layer at the Al current collector [19]. At high operating voltages, a cathode-electrolyte interphase (CEI) is also formed from organic and inorganic species [20]. Lithium hexafluorophosphate ($LiPF_6$) is the salt used in commercial LIBs. This is not because it fulfils all the criteria, but due to its well-balanced properties. It forms a stable SEI at graphite electrodes, protects the Al current collector and has relatively good ionic conductivity. Still, there are issues related to the use of this salt [19]. For one, its thermal stability is problematic. At elevated temperatures, above 60°C, there is a performance fade [21] which can be attributed to multiple factors. The SEI layer at the anode is damaged and reformed [22], there is a resistive layer formed at the cathode material due to electrolyte decomposition at the electrode, and there is also the bulk electrolyte decomposition [21]. Another issue is the operation at high voltages. When using $LiPF_6$ in electrolytes it hydrolyses, creating the toxic acid HF which deteriorates the active materials at the electrodes [23]. At high voltages, the energy barrier for this hydrolysis reaction is reduced, causing an increase in the HF formation in the cell [24].

One possibility to avoid these issues is to replace the solute. Li-imides are a group of salts extensively researched as a substitute to $LiPF_6$ [25]. Other salts, like Lithium bis(oxalato)borate, have also been investigated. Still, no salts have overall shown to possess superior properties, despite improving individual traits when replacing $LiPF_6$ [18]. One example is the use of the salt lithium bis(fluorosulfonyl)imide (LiFSI). It has a higher conductivity than $LiPF_6$ [26] and better thermal stability [27], but corrosion of the Al current collector is a major issue which prevents the use of the salt in commercial batteries [28]. Another option is the use of additives. They are used to change one property of the electrolyte without causing significant changes to the bulk properties [18]. Using ILs in electrolytes is also an option and can potentially improve the cell's properties.

2.2.3 Ionic liquids

The usual definition of ILs are compounds consisting only of ions, with a melting point below 100°C [29]. Typically, the ILs are made of relatively large organic cations and large anions, which reduces the coulombic attraction relative to ionic materials like NaCl. This is the reason for their low melting point [30]. If the melting point is below the ambient temperature it is called room temperature ILs. These can be utilised for the electrolyte of LIBs, either by adding them to the traditional electrolytes based on organic solvents or by dissolving Li-salt in the IL [31]. Some ILs that have been investigated for the electrolyte of LIBs are made up of pyrrolidinium, phosphonium and imidazolium cations together with the anions PF_6^-, $TFSI^-$, FSI^- and BF_4^- in different configurations [30] [31] [32].

There are many reasons that ILs are being investigated for use in batteries. First, their superior thermal stability relative to carbonate electrolytes. Rogstad *et al.* [33] investigated four different IL-based electrolytes and compared them to a carbonate-based electrolyte with LiFSI. During heating of the ILs, no endothermic or exothermic reactions occurred between the melting point and 200°C. The carbonate electrolyte behaves differently, with evaporation happening above 70°C. Another advantage is the larger electrochemical window observed with the use of ILs. They also have good ionic conductivity, with values between 1 and 10 mS/cm [31]. One example is that an electrolyte with 0.74m LiFSI in EMIFSI was reported to have a conductivity of 10.5 mS/cm, while the carbonate electrolyte with 0.74m LiFSI had a conductivity of 12.2 mS/cm. This proves that the conductivity of IL electrolytes can be comparable to the carbonate electrolytes [32]. The mitigation of Al corrosion when using imide-ILs instead of carbonate solvents is also a reason to investigate ILs [34]. This effect is due to the dissolution of Al ions being low without the carbonate solvents [25].

There are also problems that prevent the use of ILs in commercial LIBs. Their high cost is one significant limitation. In addition, the synthesis of many ILs is problematic, limiting the production and hindering its use in large quantities [31]. Another problem is that the performance of cells with IL-based electrolytes is lower than that of cells with conventional electrolytes at high C-rates. This is because the Li^+ diffusivity is lower, and viscosity is higher when ILs are used. So even though high ionic conductivities have been reported, this is an issue at high currents [35].

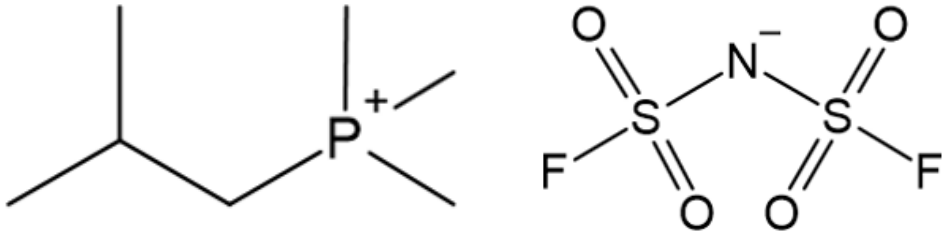

(a) **(b)**

Figure 2.3: The structure of the (a) P^+_{111i4} cation and (b) FSI^- anion.

Phosphonium-based ILs have been reported to have a lower viscosity and higher ionic conductivity than the more researched ammonium-based ILs, and simultaneously increased thermal stability is observed [36]. One such IL is trimethyl(isobutyl)-phosphonium bis(fluorosulfonyl)imide ($P_{111i4}FSI$), and the structure of its ions is shown in Figure 2.3. A $P_{111i4}FSI$ based electrolyte with 0.79m LiFSI has been found to have a large electrochemical window with oxidation beginning at 5.3 V - 5.4 V [32]. It also has good thermal stability, with a glass transition temperature of -88.1°C and reactions at -24.0°C, -18.2°C, and -4.6°C. At temperatures above this and up to 200°C, no reactions were observed, meaning no decomposition occurred in this temperature range [33].

2.3 Cathodes

2.3.1 The cathode components

A typical cathode for LIBs consists of the active material, a conductive additive, and binder. The active material is the material in which Li^+ ions are intercalated during discharge. This is typically Li-oxides, and layered, olivine or spinel-structured oxides are the most widely used [37]. A conductive additive is used because the electronic conductivity of the active material is low [38]. Without the additive, electrons can therefore not be transported to the oxide particles. The binder ensures contact between

the particles and the current collector, in addition to restraining the volumetric changes of the active material during intercalation and de-intercalation [38].

$LiFePO_4$ (LFP), LCO and $LiNi_xCo_yMn_zO_2$ (NMC) are some commercially available cathode materials [39]. LFP is an oxide with olivine crystal structure. It is used as cathode material due to its low cost, good cycling stability and thermal stability. In addition, it is environmentally friendly [40]. An issue with this material is its low operating voltage of 3.4 V, which limits the energy density [41]. LCO was a widely used cathode material, and there are many reasons for this. It is very reliable, has an excellent cycle life and has a high conductivity of both Li^+ ions and electrons. It also has a very high volumetric energy density as a consequence of the material's high density [41]. NMC are layered oxides and can have different compositions, *e.g.* $LiNi_{1/3}Mn_{1/3}Co_{1/3}O_2$ or $LiNi_{0.4}Mn_{0.4}Co_{0.2}O_2$. It contains less Co than LCO, how much less depends on the composition, and at the same time, it has a high capacity. For this reason, it is a fascinating cathode material, and it is replacing LCO [42].

The preferred choice for the carbon additive for LIB electrodes is carbon black, and the reasons for this are its high surface area, which ensures good contact, and that cell manufacturers have long-time experience with this material [43]. Other carbons can also be used as conductive additives. Graphite particles are a possibility, and graphites designed to be used as conductive carbon in battery electrodes are available [44]. There are also many other possibilities, like the use of other types of carbon, *e.g.* carbon nanotubes [45], and doping of the conductive additives [46].

There is a variety of binders used in electrodes. The most common one for cathodes is polyvinylidene fluoride (PVDF), which is dissolved in N-methyl-2-pyrrolidone (NMP) [47]. Lately, there has been an increased focus on using new binders and solvents since that can make battery production more sustainable. NMP is an organic solvent that is both environmentally hazardous and a reproductive toxin. Due to this, it is now becoming restricted in several countries [47]. But there are other options. Some binders can be dissolved in water, removing the issues related to the solvent. Three examples are carboxymethyl cellulose (CMC), styrene butadiene rubber (SBR) and alginate, which are non-toxic binders [48]. One of the reasons PVDF and NMP are still used is the low surface tension of NMP relative to water, which makes casting easier and produces more uniform electrodes. Another reason is that some cathode materials, especially those with high amounts of Ni, are very reactive towards water [47], making water an inappropriate solvent. PVDF is also known to have excellent thermal and electrochemical stability and cause good adhesion between the electrode film and the current collector [49].

2.3.2 LNMO as the cathode material

LNMO has recently gained increased interest as the active material for LIB cathodes. It has a spinel crystal structure, and there are two possible configurations. One is a face-centred spinel, called the disordered phase, and the other is a simple cubic, called the ordered phase. The disordered LNMO deviates from the stoichiometric composition, with the chemical formula $LiNi_{0.5}Mn_{1.5}O_{4-x}$. To maintain charge neutrality, some of the Mn^{4+} are reduced to Mn^{3+}. These two forms of LNMO have different electrochemical behaviour. The electrochemical curves for ordered LNMO will only have one long voltage plateau at 4.7 V, which corresponds to the redox couples Ni^{2+}/Ni^{3+} and Ni^{3+}/Ni^{4+}. Disordered LNMO will cause the voltage profile to have three distinct plateaus. One, at approximately 4.0 V, which corresponds to the Mn^{3+}/Mn^{4+} redox couple, one for the Ni^{2+}/Ni^{3+} at about 4.6 V, then another one for Ni^{3+}/Ni^{4+}, which is found at a voltage of around 4.8 V. The Ni redox couples cause two plateaus for the disordered phase because there is a solid-solution reaction for $0.5<x<1$ and a two-phase reaction for $x<0.5$. For the ordered phase, two-phase reactions occur for all $x<1$, which causes the voltage profile to have only one plateau. A two-phase reaction is the destruction and change of structure, which will limit the kinetics of lithiation and de-lithiation in the LNMO. Due to this, disordered LNMO has better structural stability than the ordered LNMO during the charging and discharging processes [8]. Based on the current knowledge regarding these two structures, the disordered structure is considered the most promising cathode material of the two crystal structures. The cycling stability of cells with ordered LNMO is worse than that of cells with disordered LNMO [10].

One advantage of LNMO is that there is no Co in the material, unlike LCO and NMC. Co is expensive, has a low abundance in the earth's crust, and is toxic [8]. In addition, it is often mined by children [9], and because of these issues, batteries without this element are therefore desired. LNMO also has a high operating voltage at approximately 4.7 V, which is the origin of its high theoretical energy density of 690 Wh/kg [10]. In addition, LNMO has been shown to have a high ionic conductivity which increases the rate of Li diffusion, and its thermal stability is superior to that of NMC [8]. Its theoretical capacity is 147 mAh/g, similar to that of other high-voltage cathode materials [10].

The technology has yet to be commercialised due to multiple problems. The Mn^{3+} present in the disordered phase will react to form Mn^{2+} and Mn^{4+}, where the former is soluble in the electrolyte [50][51]. As Mn leaves the cathode material, structural instability is increased, and this causes accelerated capacity fade. At increased tem-

peratures, the issue of Mn dissolution becomes more severe [52]. In a full cell with a graphite anode, the dissolved Mn from LNMO will be transported to the anode, where it is deposited [53]. This causes the formation of a thick SEI layer, as Mn acts as a catalyst for electrolyte decomposition. It also gives rise to Li^+ loss and delamination of the graphite from the current collector. Increased impedance, and therefore a rapid capacity decay, is then observed [54]. The high voltage also causes electrolyte oxidation, which forms a CEI layer at the cathode surface. The mechanism behind it is complicated and depends on the electrolyte composition and electrode material [8].

2.3.3 Carbon as conductive additive

The atomic structure of graphite is seen in Figure 2.4. It consists of parallel layers of graphene sheets, where each carbon atom is bound to three other carbon atoms through strong covalent bonds, with a distance between the atoms of 1.4 Å[55]. The layers are held together at a distance of 3.33 Å to 3.35 Å by Van der Waals forces [56]. The most common stacking of graphite planes is ABAB, which makes it a hexagonal crystal structure [55]. Another type of stacking is called turbostratic carbon. Here, the graphene sheets are not stacked in an ABAB pattern, but randomly with the sheets rotated about the normal of the graphene layers [57]. This also changes the interplanar distance to 3.43 Å [58]. Since graphite has strong bonds in one direction, in-plane, and weak bonds in the other direction, it has very anisotropic properties. The electrical conductivity is one property that depends significantly on the direction, with values of about $2.26 \cdot 10^4$ $\Omega^{-1}\text{cm}^{-1}$ along the basal planes, and 5.9 $\Omega^{-1}\text{cm}^{-1}$ perpendicular to these planes [59]. The anisotropy also affects how intercalation of ions into the structure happens. Due to the weak forces between the layers, intercalation generally occurs by the ions entering at the edge plane. At the edge site, ions are strongly adsorbed and can migrate to a site where they can be intercalated before moving in between the graphene layers [60].

As already mentioned, various carbons are utilised as conductive additives in LIB electrodes. The carbons differ in particle size, morphology, and crystal structure, which affects their properties. Some of these properties, which are essential for the carbon as an electrical conductor in the battery electrodes, are the electrical and mechanical properties and how it interferes with other battery components.

Carbon black is, as previously stated, widely used as the conductive carbon in LIBs. It is a group of carbons with spherical particles that form agglomerates [44]. There are many carbon blacks available, and the properties of these differ significantly. It has been found that the mean particle size of the two types of carbon black C-ENERGY

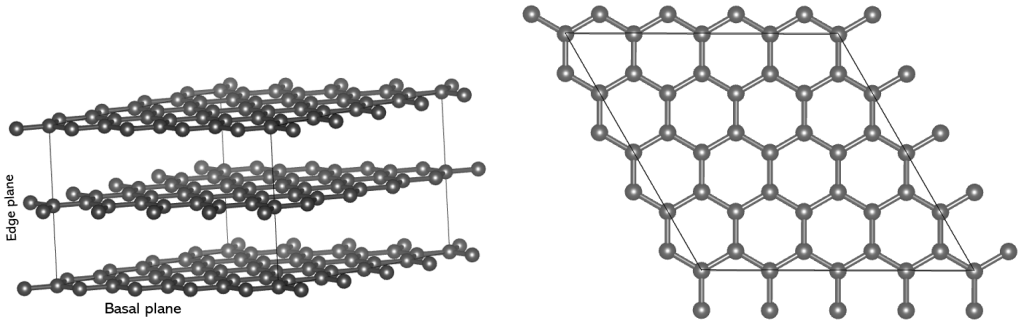

(a) (b)

Figure 2.4: The atomic structure of graphite.

Super C45 and C65 are 37 nm and 32 nm, respectively, and that the particles tend to agglomerate [44]. This small particle size causes the carbon blacks to have a surface area much larger than the active material, making it a pivotal place for electrolyte reactions. Carbon blacks have a varying degree of graphitisation, meaning that the graphitic domains of the particles have variable sizes. Still, those domains are small, leaving the particle structure amorphous [11].

Carbon black is made from hydrocarbon precursors [44]. This causes hydrogen to often be present at the edge sites at the end of the graphene layers. Other elements are also present, and oxygen is the most important of these. This can also be introduced to the carbon during production, or it can happen while storing the material. It might be a simple oxygen atom that has either replaced one of the carbons at the edge or is bound to an edge carbon. On the other hand, it might also be larger groups containing oxygen, such as carboxyl groups or hydroxyl groups [61].

Larger graphite particles can also be used as conductive carbon, given that the particle size is small enough to allow proper contact, forming a functioning electrical conductive network. In a graphite particle, there are multiple domains of graphite structure, but these domains are much larger than for carbon black. Comparing the graphite particle surface to that of carbon black, there are fewer defects, oxygen functional groups and adsorbed water molecules [62]. Typical graphites can vary in size and morphology. Some are flake-like, and others are more spherical [63].

2.4 Side reactions with the electrolyte

Unwanted side reactions between the electrolyte and the cathode is an issue, and these reactions are highly dependent on both electrolyte composition and the cathode materials. In this section, a review of reactions at the cathode will be presented.

2.4.1 Reactions with graphite

Due to few defects and oxygen functional groups present at the surface, graphite particles will experience less surface parasitic reactions than carbon black, meaning less electrolyte oxidation [62]. It is already established that ions can be intercalated into the graphitic structure, which is widely utilised at the anode, where graphite is commonly used as the active material. When using graphite as a conductive additive at the cathode side, intercalation of anions from the electrolyte occurs. Similar to Li^+ ion intercalation at the anode side, the ions go in between the graphene layers, and this happens during charging of the cell [63]. The intercalation of anions from LIB electrolytes occurs at high voltages, typically above 4.4 V [43][62][64]. The phenomenon will therefore not be an issue for LIBs with cathodes operating at lower voltages, but when using LNMO cathodes, this is a concern.

Beltrop *et al.* [64] investigated the effect of the anion size at intercalation into graphite. They used ILs with the anions FSI^-, $FTFSI^-$, $TFSI^-$, and $BETI^-$, which have different sizes. It was only found to be a correlation between the anion size and the onset potential of the intercalation for the largest anion $BETI^-$, as no intercalation was observed with this anion. Otherwise, the correlation between the onset potential and anion size was opposite of the expected, with the smallest anion having the largest onset potential. The electrolyte system can also otherwise affect intercalation. An example is the difference in intercalation behaviour when using an IL-based electrolyte compared to a carbonate-based electrolyte. When using a carbonate solution, it has been observed that the solvent can accompany the anions into the graphite, which can cause even greater damage to the graphite's crystal structure [65]. Ko *et al.* [62] reported that a sulfolane-based electrolyte with a high concentration, 5.8M, of the salt $LiBF_4$ prevented intercalation into the graphitised carbon. The behaviour of the system was attributed to the strong $BF_4^- - Li^+$ coordination at the high salt concentrations, the slow diffusion of anions in highly concentrated sulfolane electrolytes, and the formation of a stabilising CEI at the carbon.

The anion intercalation has adverse effects on the cell. It destroys the graphitic structure by increasing the interlayer distance [11]. Intercalation of $TFIS^-$ into graphite

when cycling to 5.2 V was reported to cause a volume expansion of 139% [66]. This carbon degradation creates new active sites at the surface, where reactions with the electrolyte can occur. There will be continuous electrolyte consumption through electrolyte oxidation, and the electrode resistance is therefore increased, reducing the cycling stability [62].

X-ray photoelectron spectroscopy (XPS) investigations of cycled graphite cathodes have provided information about the electrolyte reactions happening when using various electrolytes. When using LiFSI in EC:DEC, intercalation and de-intercalation were observed. In addition, no permanent CEI layer was formed. When using an IL-based electrolyte, 1M LiFSI in 1-butyl-1-methylpyrrolidinium bis-(fluorosulfonyl)imide ($Pyr_{14}FSI$), a similar trend was observed. No substantial film formation was detected, though there were indications that residues of the Pyr_{14}^{+} cation were present at the surface. This is different from the electrolyte with $LiPF_6$, where a film made from the oxidation of the solvents and decomposition of the salt was created during cycling. It was also found that this film impeded anion intercalation [67].

2.4.2 Reactions on carbon black

In general, decomposition reactions at the carbon black particles' surface are expected. The oxygen functional groups can lead to parasitic reactions with the electrolyte components. They also contribute to creating hydrophilic sites, increasing the adsorption of water molecules, which again accelerates the electrolyte oxidation [11]. The oxidation creates a film from the decomposition products, and when it covers the carbon particles, the electronic conductivity can be decreased, reducing the battery's overall performance [68].

Ko *et al.* [11] investigated acetylene black, features similar to carbon black, that had been annealed at various temperatures. Since heat treatment above 1500°C significantly promotes graphitisation, they were able to investigate the oxidation stability of carbons with different graphitisation degrees. It was reported that a low graphitisation causes irreversible oxidation reactions, while a more graphitised carbon causes more reversible reactions, which is the anion intercalation. They also found that annealing at 1200°C improves oxidation stability. This behaviour was attributed to the desorption of oxygen functional groups and adsorbed water during the heat treatment, suppressing parasitic reactions. Simultaneously, the temperature was low enough to avoid serious graphitisation.

The oxidation reactions taking place at the surface of a carbon black electrode in a half-cell with 1M $LiPF_6$ in EC:DEC as the electrolyte was investigated by Younesi *et al.* [68]. They cycled the half-cell to 4.9 V without observing the formation of a layer, but rather that the electrolyte decomposition products became integrated into the surface of the carbon particles. After 10 cycles, it was found that the solvent was partially decomposed, causing $O-C-O$, $C=O$ and carbonate species. The salt had also decomposed, causing LiF to be present.

2.4.3 Reactions observed at cathodes with both active material and conductive carbon

Yang *et al.* [69] investigated the electrolyte reactions with LNMO cathodes in cells stored at different voltages for a week. The electrolyte was 1M $LiPF_6$ in EC:DMC:DEC. The experiments showed that poly(ethylene carbonate) was formed from EC, and there was a significant difference in the composition between 4.3 V and 4.7 V, highlighting the effect of high voltage. It was also found that the salt reacted with the surface, but as the reaction appeared independent of the voltage, it was thought to be primarily thermal, not electrochemical.

Lee *et al.* [70] investigated cathodes with hollow LNMO particles as the active material after they had been cycled in half cells with 1M LiFSI in N-propyl-N-methyl-pyrrolidinium bis(fluorosulfonyl)imide ($Pyr_{13}FSI$) as the electrolyte. They found that a stable CEI layer, mitigating parasitic surface reactions, was formed with this setup. It was clear that the anion was decomposed and that the products of the reactions became part of the CEI layer. The XPS results showed that $Li-F$ and $S=O$ species were present at the electrode surface.

Until recent years, investigations of the reactions happening at the electrodes have commonly ignored or seriously underestimated the complex influence of the carbon additive. Li *et al.* [12] investigated the electrode-electrolyte interphases of a cathode with the active material $LiNi_{0.7}Co_{0.15}Mn_{0.15}O_2$, focusing on the conductive carbon, which in their experiments was the Super P carbon black. They found that even before applying voltage, there is a reaction between the electrolyte, $LiPF_6$ in EC:DEC (1:1, v/v), and the carbon. This begins the formation of a protective film. During cycling, active mass dissolution was partially suppressed as a consequence of this. One observation that is of particular interest is the exchange of interfacial species between the active material and the carbon. They found that the film originated from this phenomenon, and this "communication" between the different materials has substantial consequences for the electrochemical properties.

Carroll *et al.* [71] compared the surface of cycled electrodes of only the active material $LiMn_{2-x}Ni_xO_{4-\delta}$ (x=0.45, 0.5) with electrodes of the active material together with acetylene black and PVDF. It was discovered that the reactions involving the solvent and the $LiPF_6$ salt did not occur in the electrode containing only active material. This suggests that the active material does not contribute to the formation of the film, but rather it is the presence of carbon black, and potentially the binder, that leads to the decomposition of the electrolyte.

2.5 Electrochemical measurements

So far, theory relevant to discussing the findings of this work have been provided. Now, there will be a description of the experimental techniques used for the project.

2.5.1 Cyclic voltammetry

In cyclic voltammetry experiments, the voltage E is varied with a chosen scan rate (mV/s) between two given values while measuring the current i. The resulting plot $i(E)$ is the cyclic voltammogram, and it provides information about the reactions happening.

The Nernst equation states that

$$E = E^0 + \frac{RT}{nF}\ln\frac{c_{\text{ox}}}{c_{\text{red}}} \tag{2.10}$$

where E is the potential of the cell, E^0 is the standard potential of the species, R is the gas constant and T is temperature. n is the number of electrons taking part in the reaction, F is Faraday's constant, and c is the concentration of the given species. With this equation, the change in concentrations of reactants and products during cycling can be predicted. Nernst equation describes the equilibrium towards which the system is moving, but transport also affects the situation. In a cyclic voltammogram, current peaks will appear for reductions and oxidations. Positive peaks are from oxidation reactions, and negative peaks are from reductions. The current increases when the reaction starts to happen, and when continuing the scan, the diffusion layer at the electrode grows thicker. This slows down the transport of reactants to the surface. Eventually, the reaction will become limited by this transport, which will result in a peak in a cyclic voltammogram. Upon further cycling, diffusion is decelerated, and the current is again reduced due to less of the reaction taking place.

A reversible reaction will give two peaks in the voltammogram. One oxidation peak above E^0, and one reduction peak equally far from, but below E^0. Irreversible reactions only have one peak. The reversibility of a reaction will depend on the scan rate. If the reversible electron transfer is followed by an irreversible chemical reaction, a high enough scan rate can make it reversible due to less time for the chemical reaction to occur [72].

2.5.2 Galvanostatic cycling

During galvanostatic cycling, a constant current, decided by the C-rate, is applied. The current is applied until the cut-off voltage is reached, and then the current is reversed. Based on this experiment, many of the important battery parameters can be determined. Two values typically extracted from galvanostatic cycling are the coulombic efficiency and discharge capacity. During galvanostatic cycling, voltage profiles, as illustrated in Figure 2.5b, are obtained, and the other parameters are calculated using the equations from chapter 2.1.2.

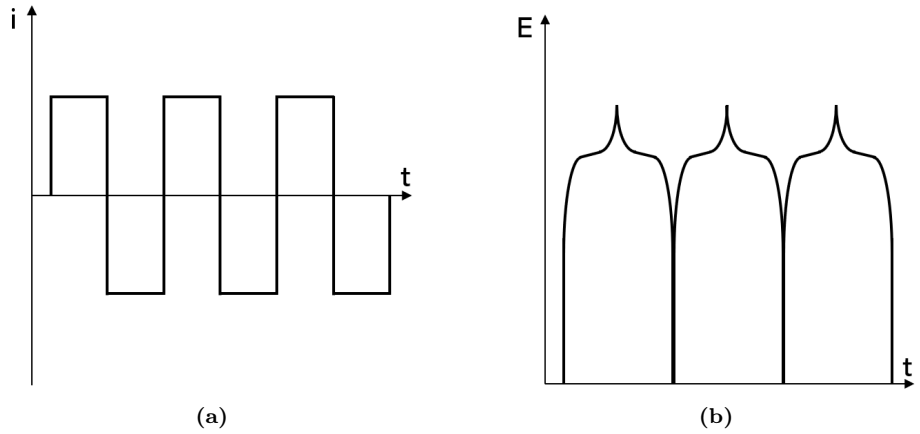

Figure 2.5: An illustration of a) the current applied and b) the voltage measured as a function of time during the cycling.

2.6 *Post mortem* characterisation

2.6.1 Scanning electron microscopy

SEM is used to create images of a sample surface. The images are obtained by sending a focused electron beam toward the sample, which creates multiple types of signals that can be detected and used to form the image. Secondary electrons, backscattered electrons, and characteristic X-rays are the most used signals for SEM. Which mode to use depends on what you are looking for. Secondary electrons, which are electrons released from the atoms of the sample due to interaction between the electron beam

and the sample, are good for seeing topographical features. This is due to their low energy, which causes the detected electrons to come from the volume close to the surface. Backscattered electrons, meaning primary electrons escaping the sample after elastic interactions, are excellent for separating which periodic elements are present in different areas of a sample. This is due to the strong correlation between the atomic number and the amount of backscattered electrons. The interaction volume is larger for backscattered than for secondary electrons, meaning the signals detected will come from a larger volume underneath the surface [73].

2.6.2 Energy dispersive X-ray spectroscopy

When an electron relaxes from a higher energy shell to a lower energy shell, energy is released in the form of X-rays. These are called characteristic X-rays, and their energy will depend on the type of atom from which they are released, as the energy difference between the shells of the atom depends on the element. Using a detector to analyse which energies the released X-rays have will therefore provide information about which periodic elements are present at the studied site [74]. By scanning an area at the sample surface, it is also possible to make a map that reveals if and where specific elements are present.

2.6.3 X-ray diffraction

XRD is a characterisation technique to extract information about the crystallites of the sample. This is done by sending X-rays towards the sample at different angles, detecting the scattered X-rays, and creating a diffraction pattern, which is a plot of the intensity of detected radiation versus the diffraction angle 2θ.

The atomic spacing of materials is usually between 2 Å and 4 Å, and for XRD the wavelength of the radiation must be smaller than the distance between the atoms, excluding all except the high-energy X-rays. During XRD, the X-rays are scattered by the atoms. For some incident angles θ, constructive interference will happen, and there will be a high-intensity signal. For other angles, destructive interference will occur, and therefore low intensities. If the sample is crystalline, there is a periodic array of atoms. When the path difference for the X-rays is equal to an integer n multiplied by the wavelength λ of the X-ray, there will be constructive interference. Figure 2.6 illustrates the principle. Bragg's law describes the condition for diffraction, stating that

$$n\lambda = 2d_{hkl}\sin\theta \tag{2.11}$$

where d_{hkl} is the distance between two parallel and adjacent planes [75].

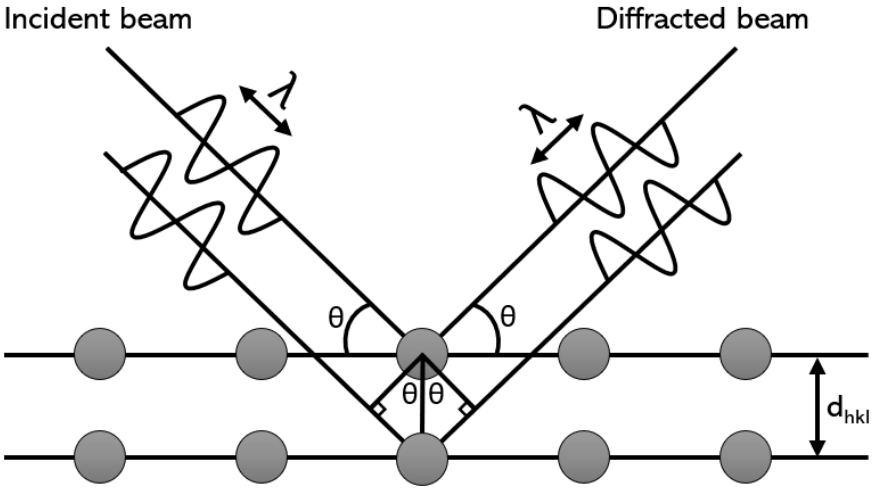

Figure 2.6: The principle of X-ray diffraction. Radiation with wavelength λ reaches the atoms with an incident angle θ and is then scattered.

Analysing the width of the diffraction peaks also provides valuable information. When a crystallite is not of infinite size, there is a limited amount of reflection planes, and the scattered X-rays close to the angles fulfilling Bragg's law are not completely cancelled out. The Scherrer equation,

$$d_p = \frac{0.9\lambda}{\beta \cos\theta} \tag{2.12}$$

relates the average crystallite size d_p to the full-width at half maximum (FWHM) value β of the diffraction peak [75]. When analysing the peak width, it is also important to be aware that microstrain in the material can broaden a peak. It is caused by crystallite defects, like dislocations, stacking faults, or point defects [76].

Two materials relevant for this work are graphite and aluminium. X-ray diffractograms for graphite have a strong peak at 26.5° and a smaller one at 54.5°. These are specific to the (002) and (004) planes, respectively [77]. Pure aluminium has peaks at 38°, 44°, 65°, 78°, 82°, 99°, 112°, 117° and 137°. The first four correspond to the (111), (200), (220) and (311), respectively [78].

2.6.4 Fourier transform infrared spectroscopy

FTIR is a non-destructive analysis that provides information about a sample's surface. Infrared radiation is sent toward the surface, then the reflected radiation is measured [79]. If the frequency of the radiation is the same as the frequency at which the molecular bonds at the surface will bend or stretch, then the radiation will be absorbed, causing less radiation with that wavelength to be measured [80]. Specific bonds between atoms vibrate at specific frequencies, so the wavelength at which absorption is

observed can provide information about which molecular bonds are present, and therefore the surface composition [81]. Table 2.1 contains molecular vibrations expected for the samples in this work and the wavenumbers where absorption peaks are previously observed.

Table 2.1: Assignment of wavenumbers to the vibrational modes they correspond to. The chemical for which the observations have been made is also given.

Vibration mode[a]	Wavenumber [cm^{-1}]
ν_a, CH_3 (DMC)	3028, 3007 [82]
ν_s, CH_3 (DMC)	2961 [82]
δ_a, CH_3 (DMC)	1458, 1453 [82]
δ_r, CH_3 (DMC)	1209, 1190, 1165 [82]
δ_s, CH_3 (DMC)	1436 [82]
$\nu, CH_3 - O$ (DMC)	973, 916 [82]
$\nu, C = O$ (DMC)	1760 [82]
ν_a, OCO (DMC)	1279 [82]
ν_s, OCO (DMC)	1120 [82]
δ_r, OCO_2 (DMC)	797, 692 [82]
$\nu_a, C - O$ (Li_2CO_3)	1480, 1430 [83]
δ (Li_2CO_3)	880 [84]
ν, CH_2 ($P_{111i4}FSI$)	3006, 2970, 2928, 2878 [85]
δ, CH_2 ($P - CH_2$ in $P_{111i4}FSI$)	1423 [85]
τ, CH_2 (LiFSI)	1307 [85]
$\nu, CH_2/CH_3$ ($P_{111i4}FSI$)	1470 [85]
ν, SF (LiFSI)	827, 810, 796 [86]
ν_a, SNS (LiFSI)	870 [86]
ν_s, SNS	759 (LiFSI) [86], 731 ($P_{111i4}FSI$) [85]
δ, SNS (LiFSI)	659 [86]
ν_a, SO_2	1373, 1413 (LiFSI) [86], 1359 ($P_{111i4}FSI$) [85]
ν_s, SO_2 (LiFSI)	1236, 1211, 1184, 1144 [86]
δ_a, SO_2	600, 585, 570 (LiFSI) [86], 566 ($P_{111i4}FSI$) [85]
$\nu, SO_2 - N - SO_2$	1234, 1178 (LiFSI) [85] 1216, 1172, 1100 ($P_{111i4}FSI$) [85]

[a] ν, stretching; δ, bending; τ, torsion; a, asymmetric; s, symmetric; r, rocking

Chapter 3

Experimental

In this section, the experimental steps performed for this work are presented. Figure 3.1 shows an overview of the work. It can be divided into four main parts. The first one is the preparation of the cell components, which is the initial pouch cell assembly and the cathode manufacture. The second step is completing the assembling of the pouch cells, and after that, the cells are cycled. Finally, post mortem characterisation of the cathodes was done using SEM, EDS, FTIR and XRD.

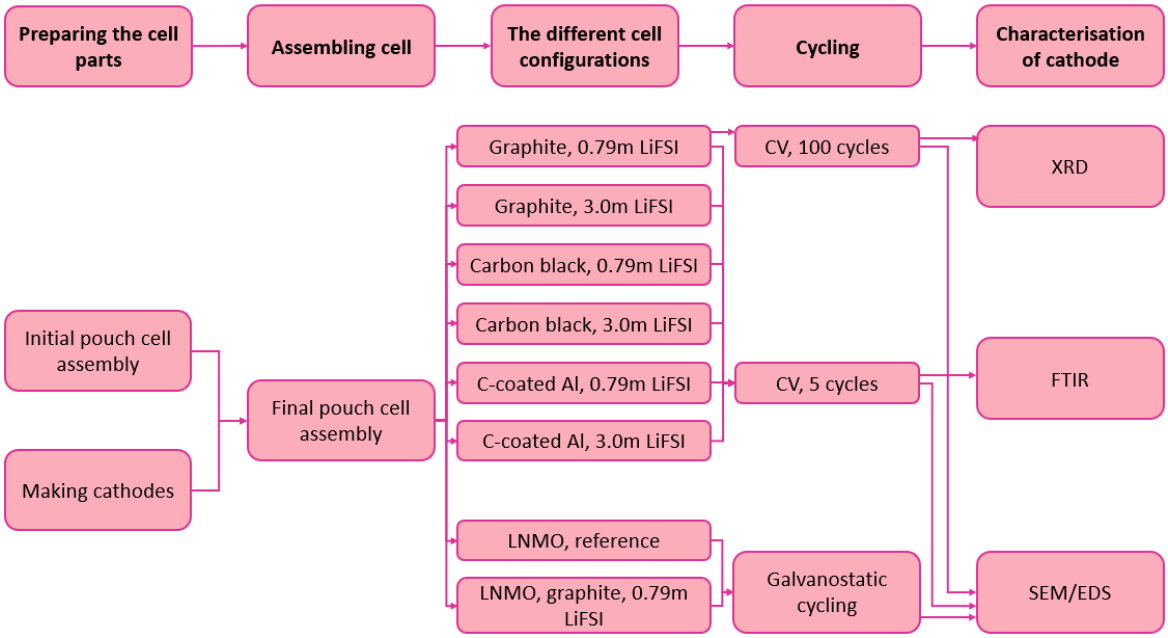

Figure 3.1: Flow chart providing an overview of the experimental work.

3.1 Materials

Table 3.1: A list of the chemicals and materials used for making the batteries.

Material	Information
LiFSI	From Solvionic
$P_{111i4}FSI$	From Ionic Liquid Technologies, purity >98%
$LiPF_6$ based electrolyte	From Sigma-Aldrich, 1M $LiPF_6$ in EC/DMC (50:50, v/v), battery grade
DMC	From Sigma-Aldrich
Na-CMC	From Sigma-Aldrich, average $M_w \sim 90000$
PVDF	From Arkema, Kynar HSV900
NMP	From Thermo Fisher Scientific, purity 99.5 %
Graphite for graphite cathodes	From Imerys, C-nergy SFG15L
Graphite for LNMO cathodes	From Imerys, C-nergy SFG6L
Carbon black for carbon black cathodes	From Imerys, C-nergy Super C45
Carbon black for LNMO cathodes	From Imerys, C-nergy Super C65
LNMO	From Haldor Topsøe
C-coated Al foil	From MTI, coating thickness of 1 µm, coating on both sides
Glass fiber separator	From Whatman
Viledon separator	From Freudenberg, FS 3002-23

3.2 Electrode manufacture

The first step of this process was to create the binder solution. For the carbon casts, the water-soluble CMC binder was used. This binder solution was made by adding de-ionised water and either 3 or 6 wt% of the CMC powder in a flask, setting it aside for stirring with a magnetic stirrer at 60°C at 500 rpm for 3 hours. For the LNMO casts, PVDF was used as the binder. The PVDF binder solution was made by mixing 5 wt% PVFD powder with the solvent NMP in a flask before stirring overnight.

The next step was to make the slurry. When making the LNMO cathodes, LNMO powder and carbon powder were first mixed together. The Retsch Mixer MM400 shaker mill was used for 2 minutes at 25 Hz. The appropriate amount of binder solution and additional solvent was added before mixing with the shaker mill proceeded. For the LNMO reference cells, the slurry composition was known, and so the liquids were added before 30 minutes of mixing at 25 Hz were done. The needed solid:liquid ratio was unknown for the other cathodes. Therefore, it was necessary to start with a modest amount of additional solvent, together with the correct amount of the binder solution, before adding a few drops at a time. After adding some solvent, the slurry was mixed for 10 minutes at 25 Hz before checking the viscosity. This process was repeated until the slurry was as desired. It was then mixed for additional 20 minutes. After mixing, it was placed in an ultrasound bath for 1 minute to remove bubbles.

Table A.1 contains the compositions of the slurries mixed. Several attempts were needed for some of the casts, but the slurry compositions of the best casts, those that were used in the cells, were as follows. Both LNMO casts had 90 wt% LNMO, 5 wt% carbon and 5 wt% PVDF. The solid:liquid ratio was different for the two casts, with a value of 0.5 for the LNMO cast with carbon black and 1.0 when using graphite as the conductive additive. Both the graphite cast with PVDF as binder and the one with CMC as binder consisted of 90 wt% graphite and 10 wt% binder. A solid:liquid ratio of 0.4 was found appropriate for both. For the carbon black cast, 85 wt% carbon and 15 wt% CMC were used, and the amount of water was adjusted to get a solid:liquid ratio of 0.16.

The slurry was cast onto the current collector using the RK K control coater 101 tape caster. The gap was 100 µm for the LNMO casts, 150 µm for the graphite casts, and both 150 µm and 50 µm were tried for the carbon black casts. The cast used for making the carbon black cathodes was the one made with the 50 µm gap. The C-coated Al foil was fixed to the tape caster with scotch tape at the top and ethanol underneath to ensure it was as flat as possible. The slurry was then applied to the

foil in an upside-down U-shape before the tape caster was turned on at the lowest velocity. The LNMO casts were dried overnight at 80°C in an oven, while the carbon casts were dried at room temperature overnight. The casts were then calendered with the MSK-HRP-MR100A calender from MTI, cut into circles with a diameter of 12 mm, and weighed.

3.3 The electrolytes

The IL-based electrolytes were mixed by combining the correct amounts of LiFSI-salt with the $P_{111i4}FSI$ IL before it was stirred with a magnetic stirrer for a few hours until the salt had dissolved. The compositions of the two electrolytes were 0.79 mol/kg and 3.0 mol/kg LiFSI in $P_{111i4}FSI$. A pre-mixed electrolyte with $LiPF_6$, as described in Table 3.1, was also used.

3.4 Initial pouch cell assembly

The initial assembly of the pouch cells was done using five different components. One was an Al foil laminated with a polymer on one side, making it non-conductive to electricity there. This foil was cut into rectangular pieces that were 12 cm × 9 cm. Cu foil and regular Al foil were cut into strips of 0.5 cm × 6 cm. These conduct current between the cell and the battery cycler. A thermal bonding film measuring 11 cm × 2 cm was also used to properly seal the top of the pouch cell. An electrical tape with a size of 10 cm × 2 cm was also used. It kept the thermal bonding film from moving during the sealing process and stopped the Al and Cu strips from being in contact with the outside of the pouch, which was electrically conductive.

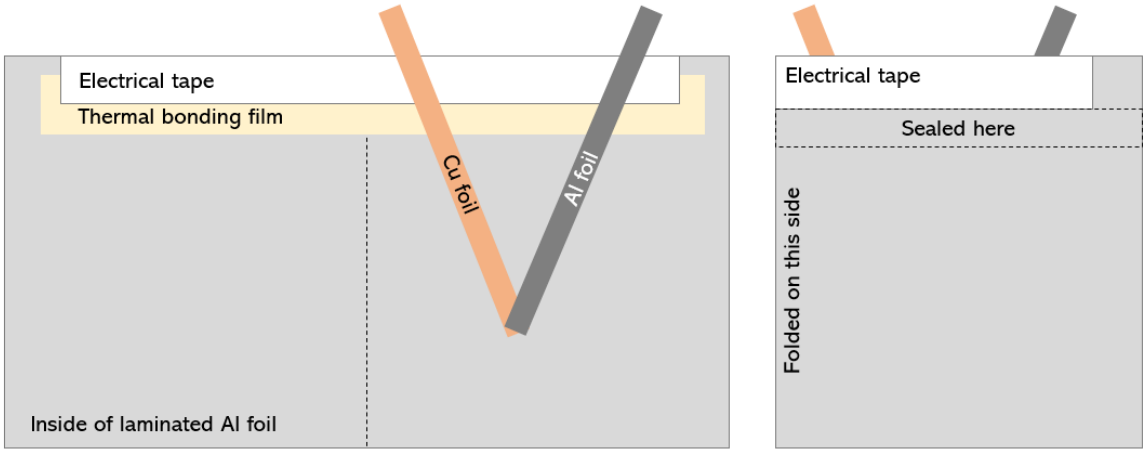

Figure 3.2: The inside and outside of the initially assembled pouch cells.

The initially assembled pouch cell is illustrated in Figure 3.2. It was made by assembling the components as shown, by placing the thermal bonding film on the laminated side of the Al foil, then attaching it with the electrical tape, which was folded over the top of the foil, to the outside. The Cu and Al foil strips were then placed inside so they overlap at the end, inside the pouch. The laminated Al foil was then folded down the middle, and the top of the pouch was sealed with the Magneta Motor sealing machine.

3.5 Final assembly of the pouch cells

The final assembly of the pouch cells was done inside a glove box from Mbraun with Ar atmosphere. The levels of O_2 and H_2O were below 0.1 ppm. The separators were dried overnight at 150°C in the antechamber before introducing them into the glove box. The cathodes were also dried in the antechamber overnight, but at 120°C.

The final assembly consisted of making the stack of electrodes, electrolyte and separators, then inserting this into the initially assembled pouch cell before sealing it. First, a circular disk of Li metal with a diameter of 14.5 mm was brushed. Next, 20 µL of electrolyte was pipetted onto this before a Viledon separator was placed on top. Then, there was another 20 µL of the electrolyte, a glass fiber separator, an additional 20 µL of electrolyte, another Viledon separator, and 20 µL more of electrolyte. Lastly, the cathode was placed on top. Figure 3.3 illustrates this sequence. The stack was placed inside the initially assembled pouch cell, with the Li towards the Cu strip and the cathode towards the Al strip. The pouch cell was then sealed at the two remaining sides with the AudionVac VMS 53 vacuum sealer, with the settings adjusted to create vacuum for 20 seconds, then seal for 5 seconds. In Table 3.2 the different combinations of cathode and electrolyte used in this work are presented, together with their abbreviations.

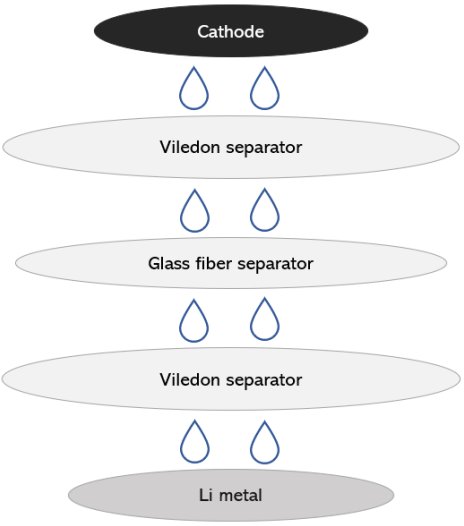

Figure 3.3: Visualisation of the stack of electrodes, electrolyte and separators.

Table 3.2: The cathode, electrolyte, and cycling program used for the different cells made for this work. The abbreviations for the different cells are also presented.

Cathode	Electrolyte	Cycling	Abbreviation
LNMO, carbon black	1M $LiPF_6$ in EC:DMC	GCPL	LNMO:ref
LNMO, graphite	0.79m LiFSI in $P_{111i4}FSI$	GCPL	LNMO:G:0.79m
Only C-coated Al	0.79m LiFSI in $P_{111i4}FSI$	CV, 5 cycles	CC:0.79m
Only C-coated Al	3.0m LiFSI in $P_{111i4}FSI$	CV, 5 cycles	CC:3m
Carbon black	0.79m LiFSI in $P_{111i4}FSI$	CV, 5 cycles	CB:0.79m
Carbon black	3m LiFSI in $P_{111i4}FSI$	CV, 5 cycles	CB:3m
Graphite	0.79m LiFSI in $P_{111i4}FSI$	CV, 5 cycles	G:0.79m
Graphite	0.79m LiFSI in $P_{111i4}FSI$	CV, 100 cycles	G:0.79m:100cycles
Graphite	3m LiFSI in $P_{111i4}FSI$	CV, 5 cycles	G:3m

3.6 Cell cycling

All cycling was done at 25°C with the BioLogic MSC-805 battery cycler and the computer program EC-Lab. Three different programs were used, and they all started with 24 hours of measuring the open circuit voltage to give the electrolyte time to wet the separators and the cathode properly. Two different cyclic voltammetry programs were used. One was 5 cycles between 3 V and 5 V, with a scan rate of 0.1 mV/s. The other program was 100 cycles between 3 V and 5 V, using a scan rate of 1 mV/s. The

last program used was galvanostatic cycling with potential limitation. This program consisted of two cycles with a current of C/10, then 50 cycles at C/2, before concluding with two more cycles at C/10. The voltage range was 3.6 V to 4.85 V.

3.7 Disassembly of the cells

The cells were disassembled inside the glove box by cutting the pouch open. The cathodes were then extracted and washed with 300 µL of DMC to remove the salt.

3.8 *Post mortem* characterisation

3.8.1 Scanning electron microscopy and energy dispersive X-ray spectroscopy

SEM imaging and EDS were done with the scanning electron microscope FEI Apreo in the cleanroom at NTNU nanolab. For imaging, both optiplan mode and immersion mode were used, both together with the in-lense T2 secondary electron detector. Optiplan mode was used for LNMO, which is slightly magnetic, and other samples at lower magnifications. Immersion mode was used for the high-magnification imaging of carbon black cathodes. The acceleration voltage was set to 3 kV and the emission current to 0.1 nA for both modes. A working distance of 10 mm was used together with optiplan mode, and it was set to 4.6 mm when using immersion mode. For EDS, standard mode and the EDX Oxford Xmax 80 mm^2 detector was used. The working distance was 10 mm, the acceleration voltage was 5 kV, and the emission current was 0.1 nA.

3.8.2 Fourier transform infrared spectroscopy

For the FTIR measurements of the cathodes, the Bruker Vertex 80V attenuated total reflectance (ATR)-FTIR was used, together with the computer program Opus. As components formed at the surface can react with the oxygen in the air, the samples were mounted to the ATR disk in the glove box. This procedure is shown in Figure 3.4. First, the sample was attached to the disk with a small sticker to ensure it did not move during the following steps. Then, a piece of Al foil was placed on the sample. Lastly, contact paper was applied to seal out the air. The Al foil was used because it is not for sure that the contact paper is impermeable to oxygen.

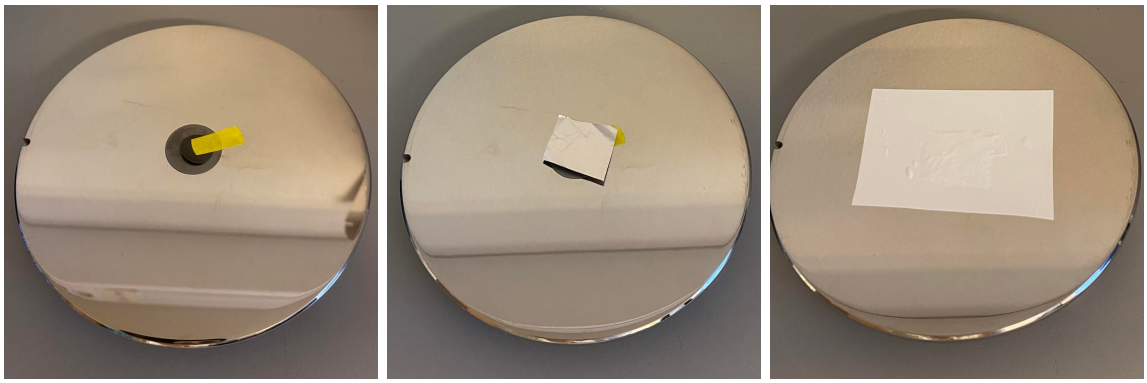

(a) (b) (c)

Figure 3.4: How the samples were mounted to the disk for FTIR measurements.

For the measurements, the pristine cathode materials were used as background. The scan range was set to 4000 cm^{-1} to 350 cm^{-1}, the aperture to 6 mm, the scanner velocity to 10 kHz and the resolution to 4 cm^{-1}. The number of scans was set to 100.

3.8.3 X-ray diffraction

The samples were first mounted to the backloader XRD sample holder by attaching the sample to a small piece of glass using vacuum grease. This piece of glass was then attached to the sample holder with more vacuum grease. A larger glass plate was used to push the sample down, making it even with the edge of the holder.

The Bruker D8 A25 DaVinci X-ray Diffractometer with Bragg-Brentano geometry was used for the XRD analysis. The divergence slit was so that the illuminated length on the sample was constantly 6 mm. The machine used Cu Kα radiation. A 2θ range from 15° to 120° was used, and the step size was 0.00818°.

Chapter 4

Results

4.1 Carbon cathodes

4.1.1 Cyclic voltammetry

To investigate the electrochemical behaviour of the different cells, cyclic voltammetry between 3 V and 5 V was performed (Figure 4.1 to 4.4). The cut-off potential is selected while taking into account its application specifically for LNMO cathodes. Four types of cells with a graphite cathode were cycled; G:0.79m with CMC as the binder (Fig. 4.1a), G:0.79m with PVDF as binder (Fig. 4.1b), G:3m with CMC binder (Fig. 4.1c) and G:0.79m:100cycles with CMC as binder (Fig. 4.2). The voltammograms of the cells cycled 5 times show multiple oxidation and reduction peaks. There are three oxidation and three reduction peaks, but they are less distinct for the G:3m cell compared to the others. The oxidation peaks are higher during the first cycle than the other cycles, while the reduction peaks are more similar for all cycles.

To investigate the effect of extended cycling on the graphite cathodes, a cyclic voltammetry program with 100 cycles at 1 mV/s was also done (Figure 4.2). Compared to a scan rate of 0.1 mV/s, the cyclic voltammetry scans of higher scan rate exhibit only two distinguishable peaks. One is a distinct oxidation peak, and the other is the beginning of an increasing current when the maximum voltage is reached. For the reduction reactions, there is one peak with a shoulder. No particular change is observed between the second and the hundredth cycle.

The cyclic voltammograms of CB:0.79m and CB:3m can be seen in Figure 4.3. Here, the only oxidation peak is the one at the cut-off voltage of 5 V. The sharp peak is evidence that the currents would keep increasing if the voltage was increased further.

No reduction peaks are present, but some fluctuations in the graphs can be observed. In Figure 4.4, the cyclic voltammograms for a) CC:0.79m and b) CC:3m are shown. These exhibit mostly oxidation reactions, but small reduction peaks are also seen.

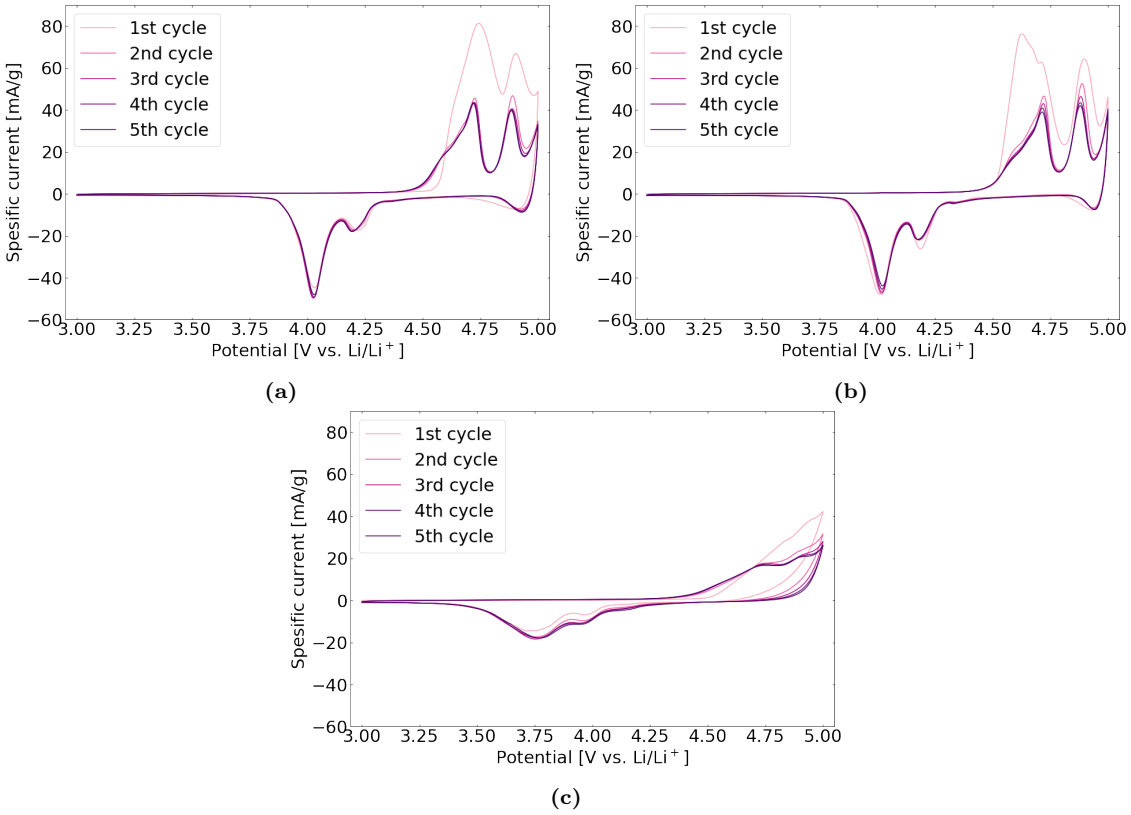

Figure 4.1: Cyclic voltammograms for the half cells a) G:0.79m with CMC binder, b) G:0.79m with PVDF binder and c) G:3m with CMC binder.

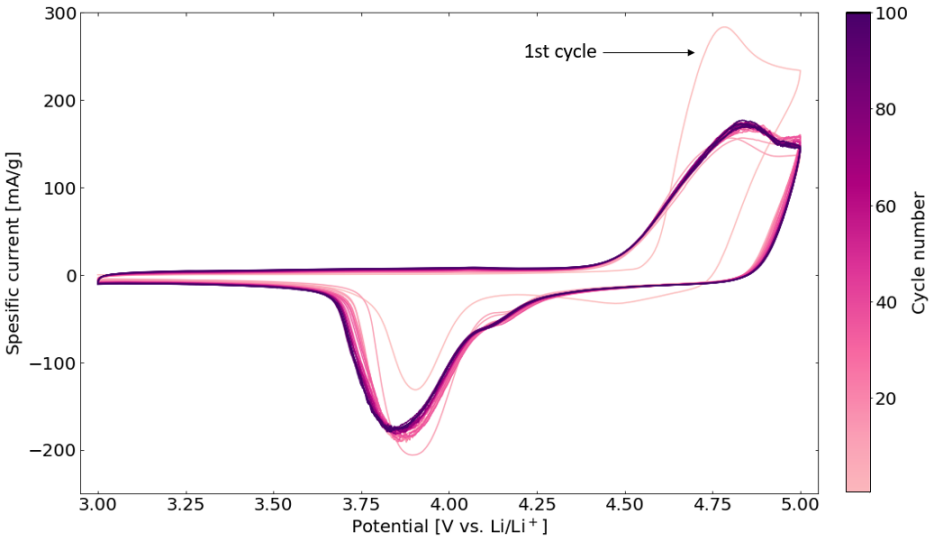

Figure 4.2: Cyclic voltammogram for G:0.79m:100cycles. Scan rate was 1mV/s. The first cycle is plotted, and then every fifth cycle.

Table 4.1 contains the average onset potentials observed for the different cells. This value is here defined as the potential at which the specific current reaches a value of 10 mA/g. PVDF as the binder in G:0.79m cells causes the onset potential to be 4.53±0.00 V with a 95% confidence interval, and using CMC increases this value to 4.58±0.01 V. When using PVDF, the potential at which the reactions are initiated is the same for all cycles. With CMC, the reactions start at a higher potential during the first cycle than the next cycles. Table B.1 provides the onset potential for the remaining cycles for G:0.79m with CMC. This is 4.55±0.00 V, still higher than for the cells with PVDF. For G:3m, the average onset potential is 4.62±0.03 V, while it is 4.59±0.02 V and 4.65±0.05 V for CB:0.79m and CB:3m, respectively. In comparison, they are 4.47±0.05 V and 4.52±0.03 V for CC:0.79m and CC:3m. These results demonstrate that the electrolyte with 3m LiFSI cause the onset potential to shift to higher voltages, compared to when the electrolyte contains 0.79m LiFSI. It is also found that the onset potential is higher for carbon black cathodes than graphite cathodes when using the same electrolyte in both cells.

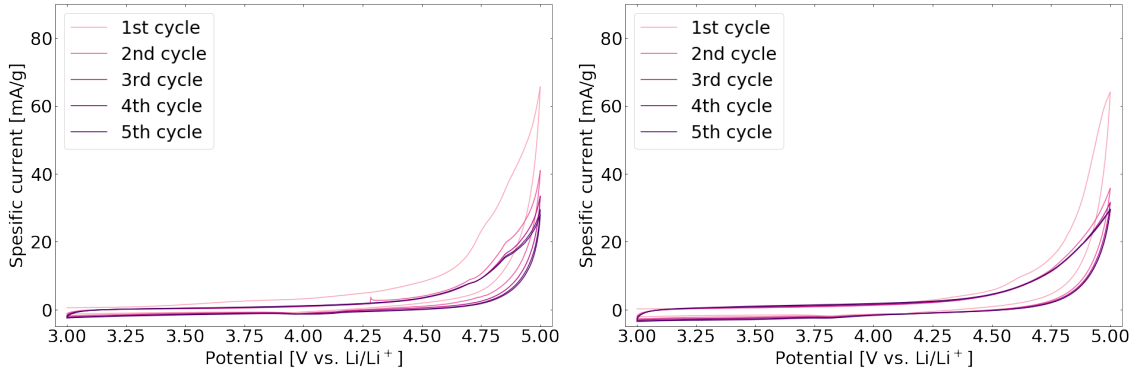

(a) **(b)**

Figure 4.3: Cyclic voltammograms for the a) CB:0.79m and b) CB:3m cells.

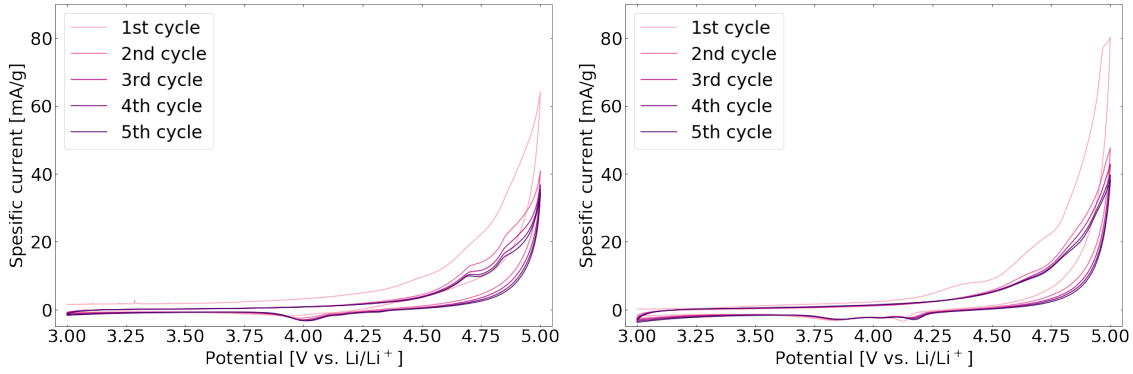

(a) **(b)**

Figure 4.4: Cyclic voltammograms for a) CC:0.79m and b) CC:3m.

The cumulative charge was also calculated, by integrating the specific current as a function of time (Table 4.2). It is therefore a measurement of the oxidations, the positive currents, subtracting the reductions, the negative currents. A background current was subtracted, both for negative and positive currents. For most cells, this is the approximate current at 3.5 V, though the current differs some for each cycle. The exception is for the G:3m cells, where reduction reactions still happen at 3.5 V. Therefore, the flat area around 4.5 V was used instead. The average cumulative charge for CB:0.79m is smaller than that of CB:3m, while the one for G:0.79m is larger than for G:3m. But it is observed that the cumulative charge is always larger for cells with carbon black cathodes than for cells with graphite cathodes. For the cells with graphite, the reversibility of the reactions was also calculated (Table 4.3). This is the area underneath the reduction peaks in the cyclic voltammograms, divided by the area underneath the oxidation peaks. The background current is subtracted. On average, the reversibility of G:0.79m is 63.9%, and it is 58.1% for G:3m, with values for individual G:0.79m cells always being higher than that of all G:3m cells. The G:0.79m:100cycles cells have a poor reversibility of 25% during the first cycle, but after a few cycles it stabilises, with the average reversibility being 81.3% for the 10th cycle and 83.7% for the 100th cycle.

During disassembly of the CB:3m and G:3m cells, it was discovered that salt had precipitated during cycling (Figure 4.5). The salt was observed at the cathodes, between the separators, and at the Li anode. Damage to the graphite cathode surface was also observed. This salt precipitation was not observed at the CC:3m cathode.

Table 4.1: Average onset potentials for the cells investigated.

Cell	Onset potential [V]
G:0.79m (PVDF)	4.53±0.00
G:0.79m (CMC)	4.58±0.01
G:3m	4.62±0.03
CB:0.79m	4.59±0.02
CB:3m	4.65±0.05
CC:0.79m	4.47±0.05
CC:3m	4.52±0.03

Table 4.2: Cumulative charge based on cyclic voltammetry measurements for individual cells, and the average for the different types of cells. All cells were cycled 5 times.

Cell	Cumulative charge [C/g]	Average values [C/g]
G:0.79m	262.7	
G:0.79m	263.3	266.2
G:0.79m	272.7	
G:3m	254.8	
G:3m	234.4	232.1
G:3m	207.1	
CB:0.79m	608.7	
CB:0.79m	581.9	558.8
CB:0.79m	485.9	
CB:3m	464.4	
CB:3m	696.2	578.0
CB:3m	573.3	

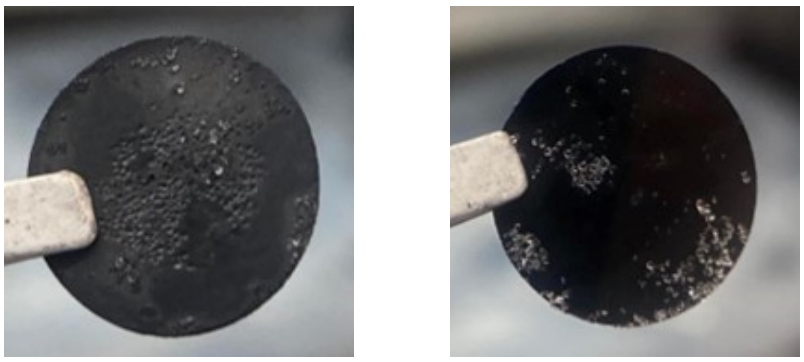

(a) **(b)**

Figure 4.5: Salt crystals formed during cycling with the electrolyte containing 3m LiFSI. Shown at a) graphite electrode and b) carbon black electrode.

Table 4.3: Reversibility of the observed oxidations for individual cells. Due to the large difference in behaviour during the first cycle compared to the others, values for the first cycles and the last cycles are also given.

Cell	All cycles [%]	1st cycle [%]	10th cycle [%]	Last cycle [%]
G:0.79m	64.4	39.5		79.8
G:0.79m	64.0	38.9		79.9
G:0.79m	63.2	37.6		79.8
G:0.79m:100cycles	78.0	26.6	77.7	80.4
G:0.79m:100cycles	83.4	29.1	83.7	85.5
G:0.79m:100cycles	83.2	31.0	82.5	85.2
G:3m	58.7	35.3		73.9
G:3m	58.1	34.2		73.1
G:3m	57.4	32.9		72.3

4.1.2 Scanning electron microscopy

Post mortem SEM imaging was done for the different samples to investigate the surface after cyclic voltammetry scans. In Figure 4.6, the pristine C-coated Al, CC:0.79m, and CC:3m can be viewed. The pristine current collector has a thin carbon layer consisting mainly of nanoparticles, though some larger particles are also present. Some of the aluminium underneath is still visible. After cycling, the surface is covered with a surface film. It is also found that the film is more even at the CC:3m cathode compared to the one at the CC:0.79m cathode since the features of the carbon are less prominent. This indicates a thicker film at the CC:3m cathode.

For the carbon black cathodes (Figure 4.7), the aluminium is not visible through the carbon. After cycling of the CB:0.79m cell, it is distinctly different from the pristine sample. A film has formed, both creating a network between the individual particles and partially covering the particles. The C:3m cathode has a different appearance. No film covers the particles, but again a network appears to have been formed between them. It appears as if the particles cluster together.

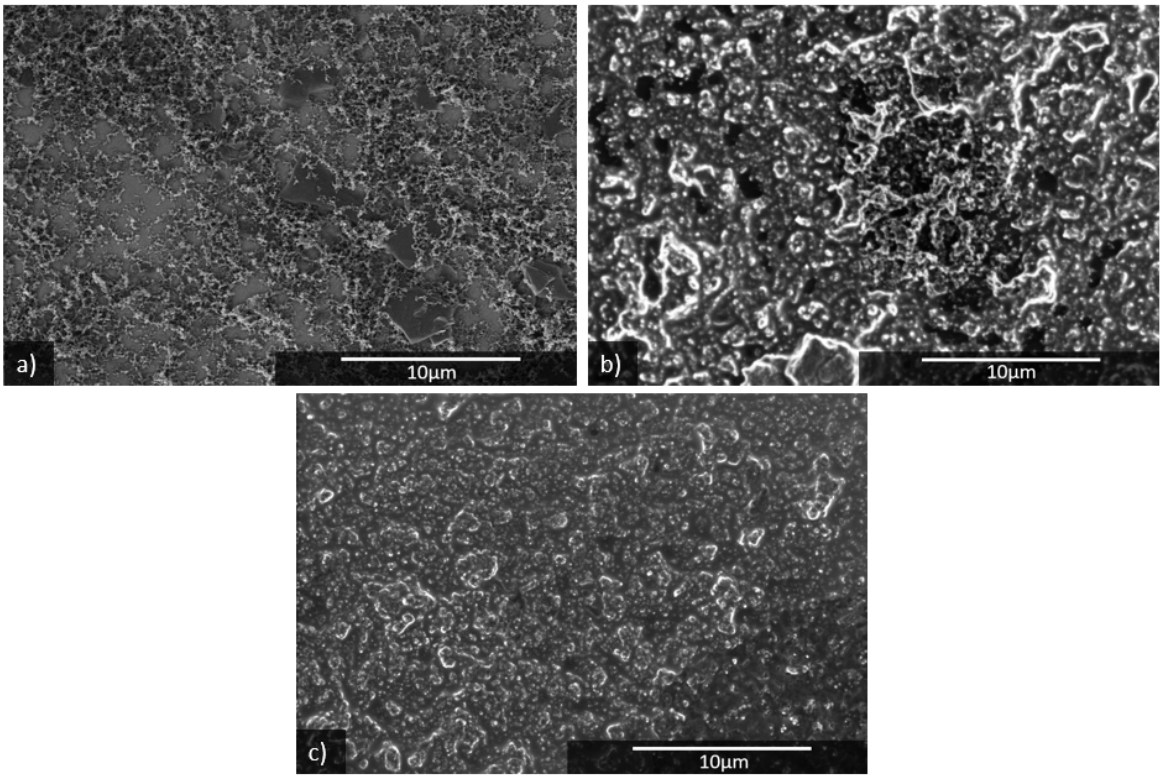

Figure 4.6: SEM images of a) pristine C-coated Al foil and the surfaces of the b) CC:0.79m and c) CC:3m cathodes after five cyclic voltammetry scans.

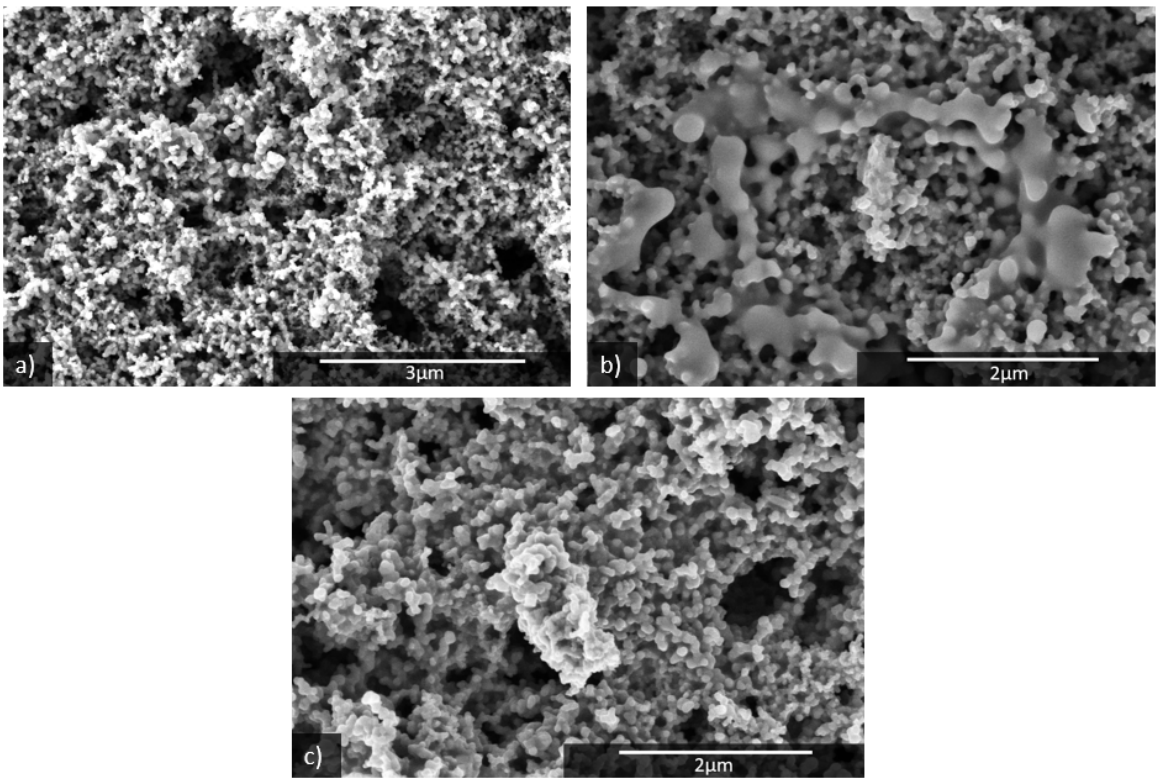

Figure 4.7: SEM images of a) the pristine carbon black cathode and the surfaces of b) CB:0.79m and c) CB:3m cathodes after five cyclic voltammetry scans.

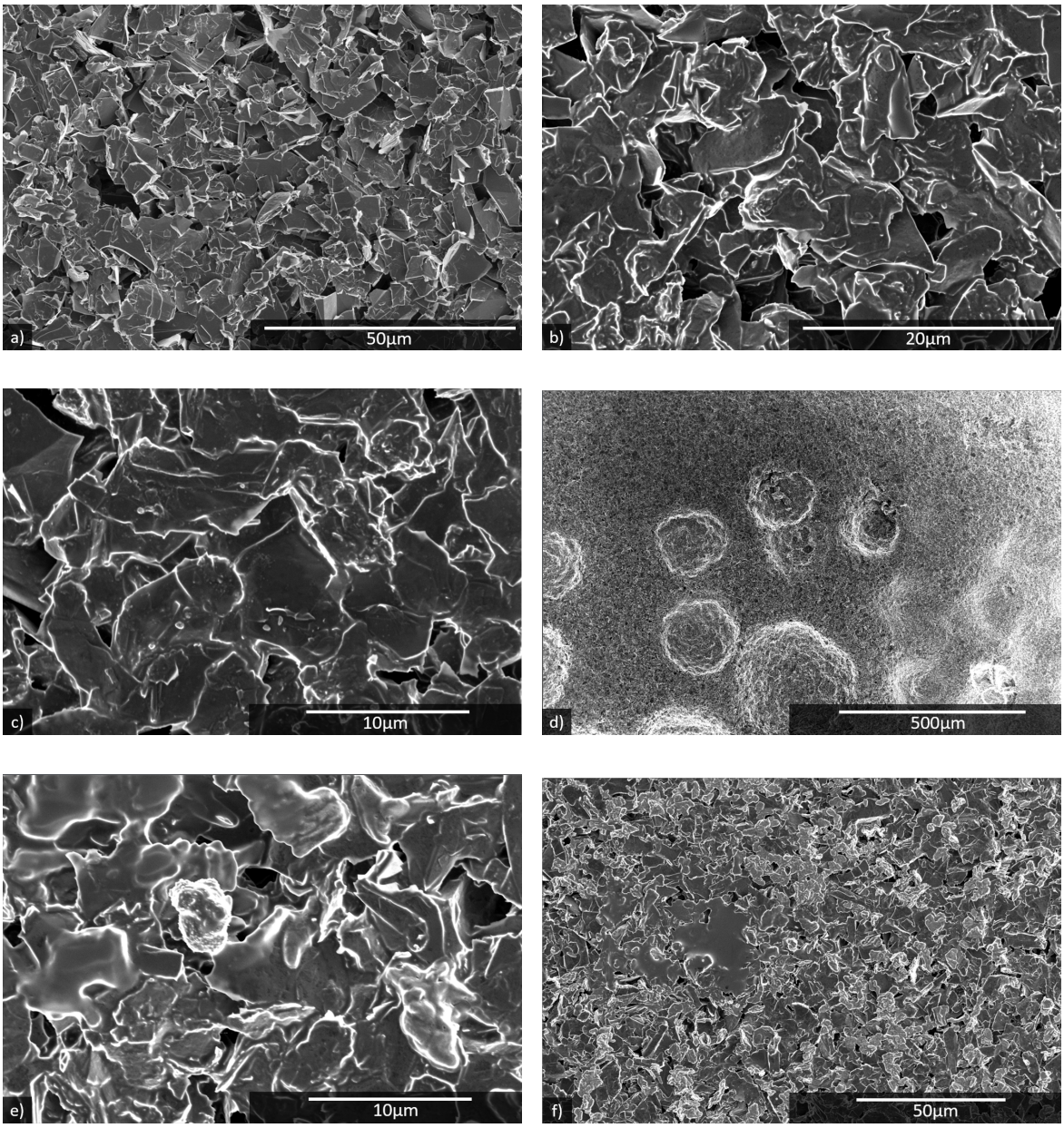

Figure 4.8: SEM images of a) the pristine graphite cathode, b) G:0.79m, c,d) G:3m, e,f) G:0.79m:100cyces.

Figure 4.8 contains the SEM images of graphite cathodes. The first image is the pristine cathode. The varying size and sharp edges of the particles are observed here. In Figure 4.8b, the G:0.79m cathode is shown. While the particles were easily distinguishable at the pristine sample, identifying single particles is now more challenging. A film has formed at the surface, covering the particles and making their edges appear softer. The same is seen for the G:3m cathode in Figure 4.8c. Figure 4.8d reveals indentations in the G:3m cathode surface, as also observed during the disassembly of the cells. In Figures 4.8e and 4.8f, SEM images of the G:0.79m:100cycles electrode surface are

presented. Again, a film is present at the surface. In addition, there are now smaller particles with a rougher surface.

4.1.3 Energy dispersive X-ray spectroscopy

EDS maps and spectrum for the G:0.79m cathode are found in Figure 4.9. The elements carbon, oxygen, phosphorous, fluorine, sulfur and nitrogen are present, as seen from the spectrum. While the phosphorous and sulfur are evenly distributed across the surface, the maps of the other elements have areas where the signal is lower. This is in the space between the graphite particles. Figure 4.10 provides the EDS information for an area at the G:0.79m:100cycles cathode. Again, the same elements are present. However, the distribution of carbon, oxygen and sulfur differs from that of the G:0.79m cathode. As previously stated, this cathode has some smaller particles with a more uneven surface, in addition to the particles with features similar to those of the pristine sample. The EDS reveals that more oxygen and sulfur are found at these rougher particles compared to the other areas. The phosphorous map is even, and the fluorine and nitrogen maps are mostly even, except for the reduced intensity in the cracks between some particles. The EDS maps and spectrum for the G:3m cathode (Figure 4.11) reveal that all elements are evenly distributed at this sample surface. Here, there is more phosphorous than nitrogen, unlike the G:0.79m and G:079m:100cycle cathodes, where the opposite is observed. At both the CB:0.79m cathode (Figure 4.12) and CB:3m cathode (Figure 4.13) all elements are present, and they are evenly distributed, the exception being that less carbon and oxygen are observed in the crack at the CB:0.79m cathode. Similarly, as for the graphite cathodes, there is more nitrogen than phosphorous after cyclic voltammetry scans with the electrolyte containing 3m LiFSI, and the opposite is seen for the CB:0.79m cathode. The amount of nitrogen observed for the CB:0.79m is minimal. Figure C.1 in appendix C presents the EDS spectra and layered images of a pristine graphite cathode and carbon black cathode. Comparing the EDS graphs of cycled samples to these, one can observe that cycling reduces the signal from carbon and increases that of oxygen. The behaviour is similar for the carbon black and graphite cathodes.

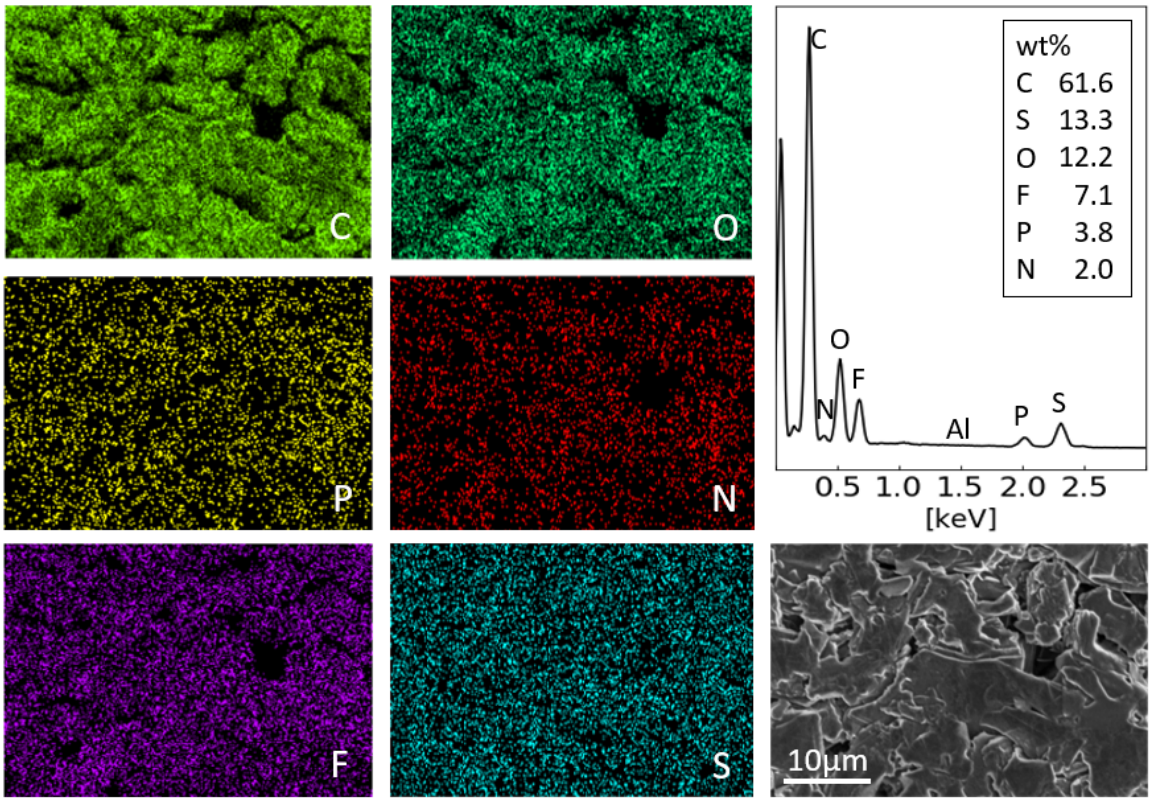

Figure 4.9: EDS maps and spectrum for a G:0.79m cathode.

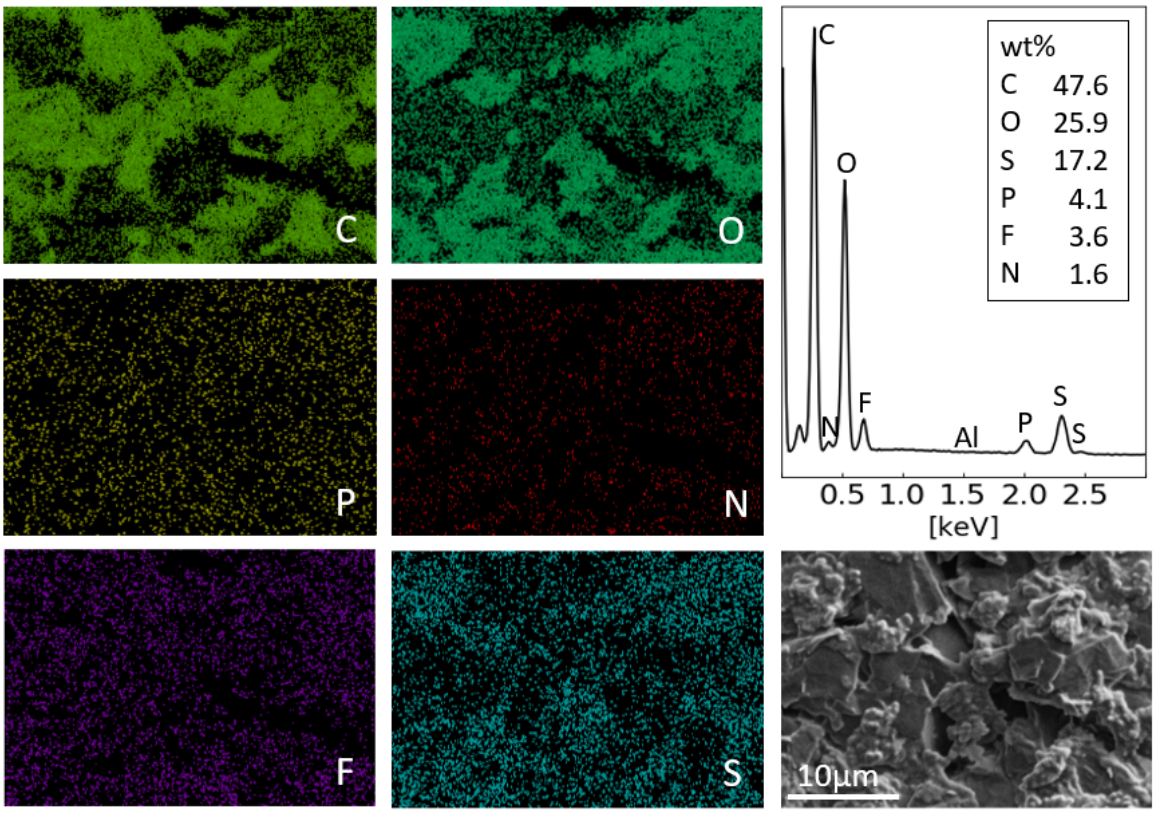

Figure 4.10: EDS maps and spectrum for G:0.79m:100cycles.

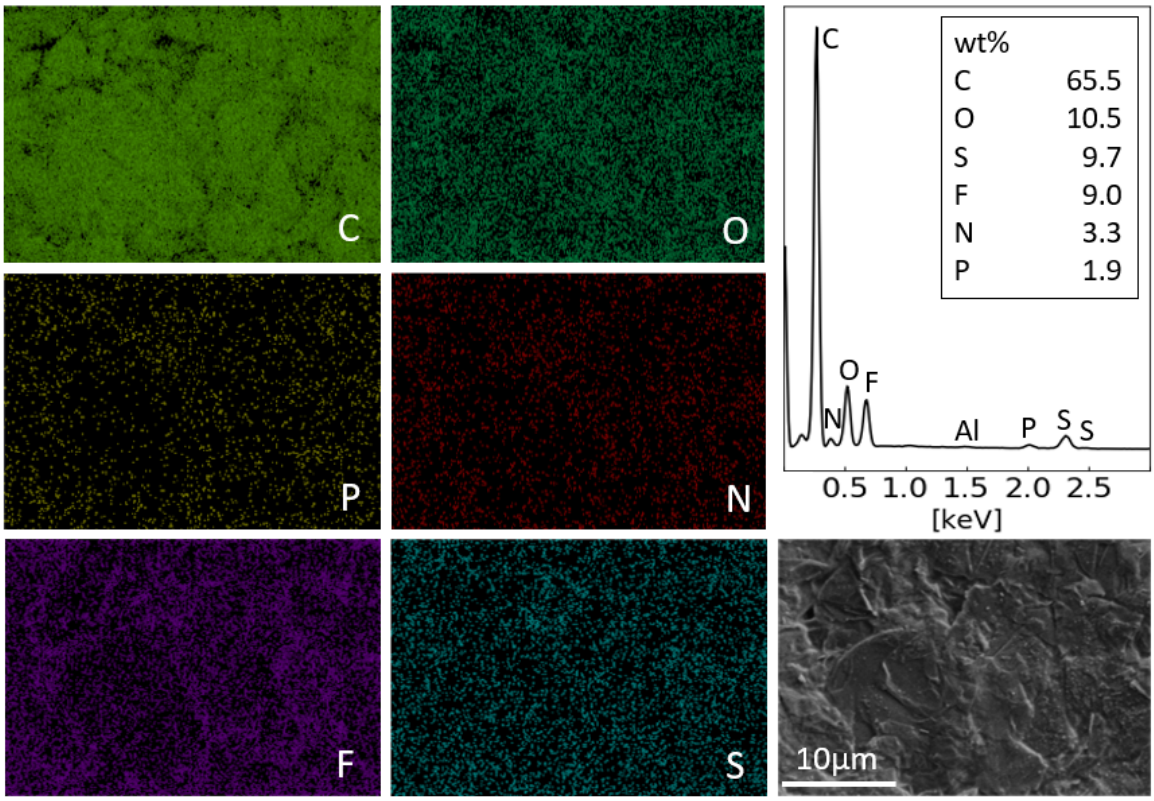

Figure 4.11: EDS maps and spectrum for a G:3m cathode.

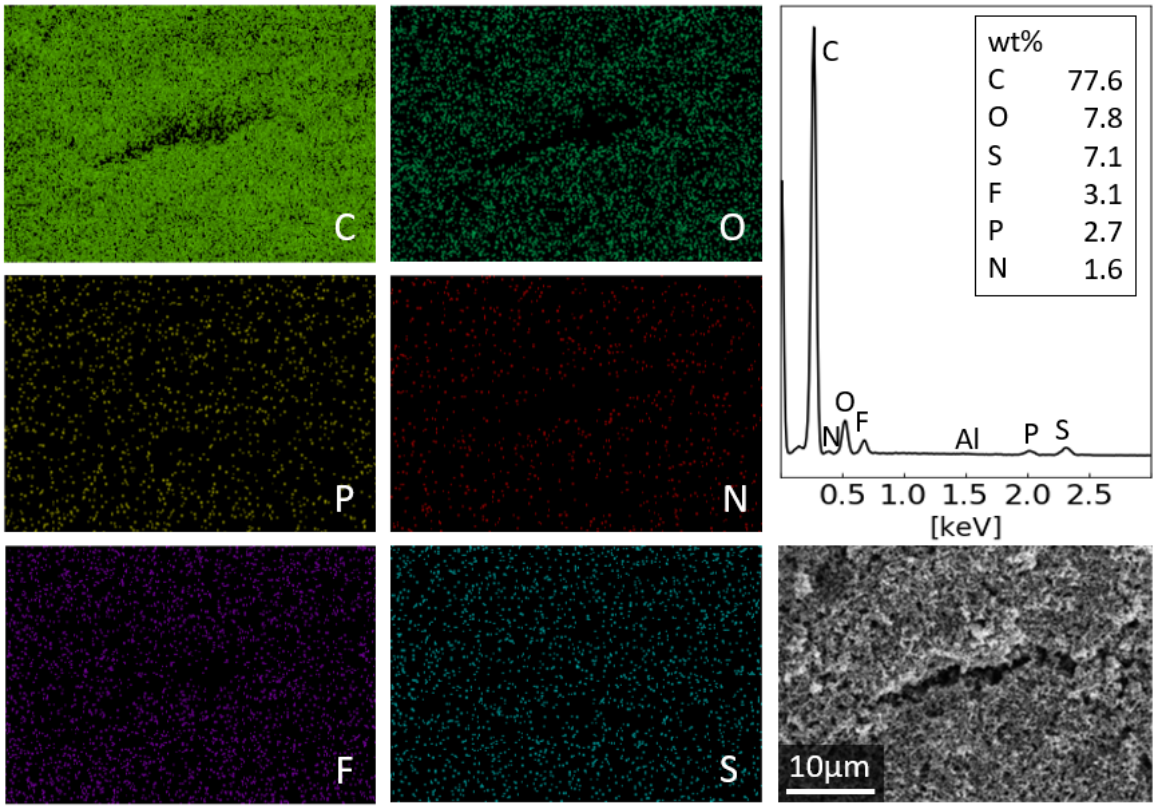

Figure 4.12: EDS maps and spectrum for a CB:0.79m cathode.

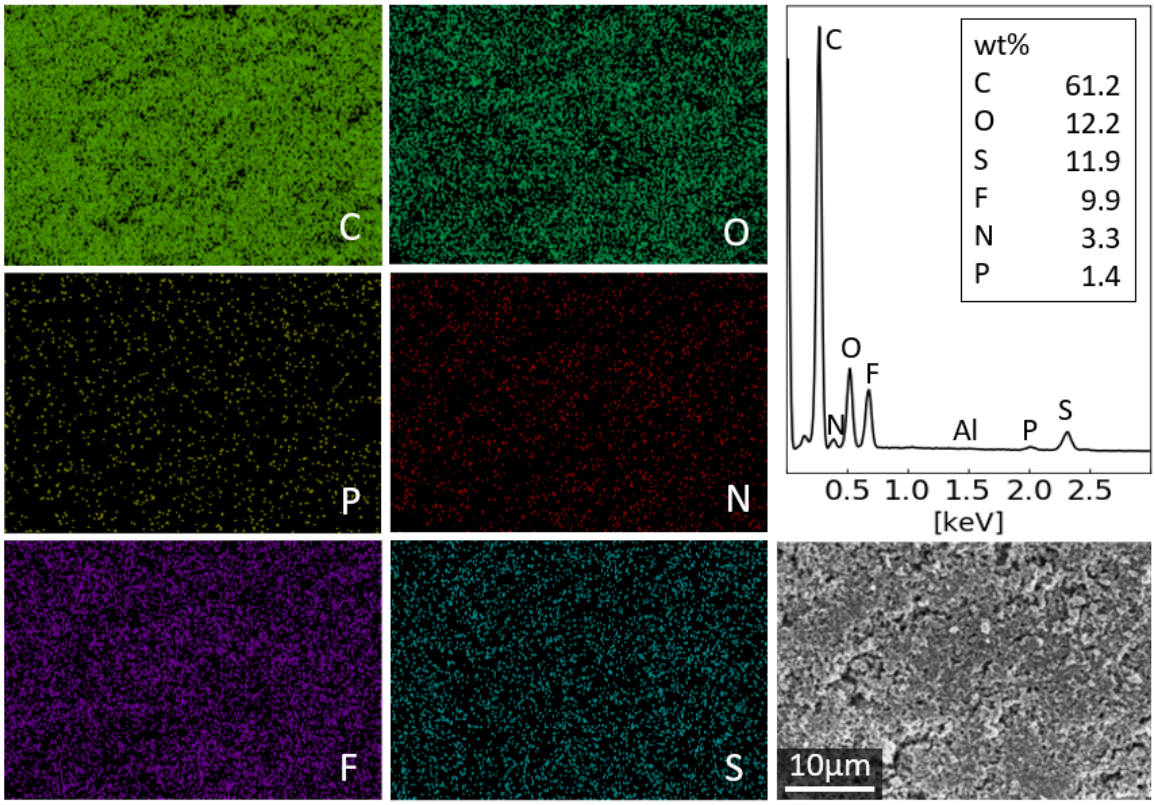

Figure 4.13: EDS maps and spectrum for a CB:3m cathode.

4.1.4 Fourier transform infrared spectroscopy

The absorbance spectra of the different cathodes are presented in Figure 4.14, and Table 4.4 contains the peaks observed for all samples, together with the molecular vibrations that have been assigned to them. All assignments are based on Table 2.1. Not all peaks have been assigned to a vibration, as it is unknown what causes some of the peaks. It is important to consider that the scale of the absorbance is different for the six panels of the figure and that intensities can not be compared across different panels.

There are few differences between the FTIR spectra of the G:0.79m and G:3m cathodes. The intensities are marginally higher for G:3m, and a couple of peaks are only observed for one of the samples, but otherwise, they are similar. Two peaks are present at high wavenumbers, around 3000 cm^{-1}. These are from the stretching of CH_2 or CH_3. A peak at 1408 cm^{-1} can be from the bending of CH_2, but it is unsure as it might also be attributed to the SO_2 asymmetrical stretching. There is also a peak at 1309 cm^{-1} that is from the torsion of CH_2 bonds. A peak for OCO stretching is observed. Both cathodes have peaks from both symmetrical and asymmetrical stretching of SNS. One peak that can correspond to the SNS stretching, at 877 cm^{-1} is overlapping with

the bending of Li_2CO_3. The only peak that can come from SF is at 798 cm^{-1} and is only observed for the G:3m electrode. However, this peak can also be attributed to bending of OCO_2. Of the three vibrational modes for SO_2, both asymmetrical stretching and asymmetrical bending occur. Symmetrical stretching might happen, but $SO_2 - N - SO_2$ stretching and CH_3 bending are attributed to the same wavenumbers, making the results inconclusive. Due to this, the presence of $SO_2 - N - SO_2$ is also uncertain.

Even though the general features of the spectra for CB:0.79m and CB:3m are similar, some differences are found. There are more peaks for the CB:3m cathode, but also some peaks only found for the CB:0.79m cathode. No peaks are present at the high wavenumbers, but there are still peaks indicating the presence of organic species. The peaks at 1411 cm^{-1}, 1303 cm^{-1}, 1210 cm^{-1}, 1168 cm^{-1} and 790 cm^{-1} can come from vibrations of CH_3 or CH_2. However, the peak at 1303 cm^{-1}, found only for the CB:0.79m cathode, is the only one with no other possible origin. This is also why it is unsure if a peak corresponds to the symmetrical SO_2 stretching. Still, there is a peak for SO_2 asymmetrical bending for CB:3m, and evidence of the asymmetrical stretching of SO_2 for both cathodes. The peaks of $SO_2 - N - SO_2$ are also affected by the overlapping of vibrational modes for the different species, but for the CB:0.79m cathode, there is a peak with no other known possible origin than its stretching. The peaks at 823 cm^{-1}, 810 cm^{-1} and 790 cm^{-1} can be attributed to the stretching of SF, but the latter might also come from rocking of OCO_2. For the SNS vibrations, both symmetrical and asymmetrical stretching is observed.

The FTIR spectra of CC:0.79m and CC:3m cathodes have similar features. Only one peak is observed for the CC:3m and not for the other cathode, and apart from that, they have the same peaks. The difference is in the intensities, which are much higher for CC:3m than for CC:0.79m. The relative peak intensities are also similar for both samples. These samples have four peaks around 3000 cm^{-1}, which are attributed to organic species, more specifically the stretching of CH_2 and CH_3. They also have a peak corresponding to the CH_2 torsion. Two peaks can come from the rocking of CH_3, but both can also be from the $SO_2 - N - SO_2$ stretching, and one can also be caused by the SO_2 symmetrical stretching. There are peaks for both the symmetrical bending and asymmetrical stretching of SO_2. There are no peaks from either OCO_2 or OCO, and no from SF stretching. SNS symmetrical stretching is observed, but no other indications of this chemical component.

Table 4.4: Peaks observed in the FTIR spectra for the different samples. The peaks are also assigned to chemical bonds, where their nature is known. Based on Table 2.1 in section 2.6.4.

Peak [cm^{-1}]						Assignment
CC:0.79m	CC:3m	CB:0.79m	CB:3m	G:0.79m	G:3m	
3005	3005					$\nu_a(CH_3), \nu(CH_2)$
2968	2968			2968	2968	$\nu_s(CH_3), \nu(CH_2)$
2927	2927			2927	2927	$\nu(CH_2)$
2880	2880					$\nu(CH_2)$
				1581	1581	
	1470					$\nu(CH_2/CH_3)$
1425	1425		1411	1408	1408	$\delta(CH_2), \nu_a(SO_2)$
1377	1377					$\nu_a(SO_2)$
1360	1360	1371	1363	1364	1364	$\nu_a(SO_2)$
		1349				$\nu_a(SO_2)$
1307	1307	1303		1309	1309	$\tau(CH_2)$
			1234	1225	1234	$\nu_s(SO_2), \nu(SO_2 - N - SO_2)$
1219	1219	1211	1210	1198	1209	$\nu_s(SO_2)$, $\nu(SO_2 - N - SO_2)$, $\delta_r(CH_3)$
1174	1174	1168	1168			$\nu(SO_2 - N - SO_2), \delta_r(CH_3)$
				1122	1130	$\nu_s(OCO)$
1112	1112		1110			
		1096				$\nu(SO_2 - N - SO_2)$
1081	1081	1075	1081	1084	1084	
980	980	975	975	985	985	
959	959	951	951	966	965	
			896			
				877	877	$\nu_a(SNS), \delta Li_2CO_3$
			865	852	865	$\nu_a(SNS)$
842	842		847			
		823				$\nu(SF)$
			810			$\nu(SF)$
			790		794	$\nu(SF), \delta_r(OCO_2)$
				778	778	
755	755		752	751	751	$\nu_s(SNS)$
				590	600	$\delta_a(SO_2)$
576	576		582	581		$\delta_a(SO_2)$
			559			

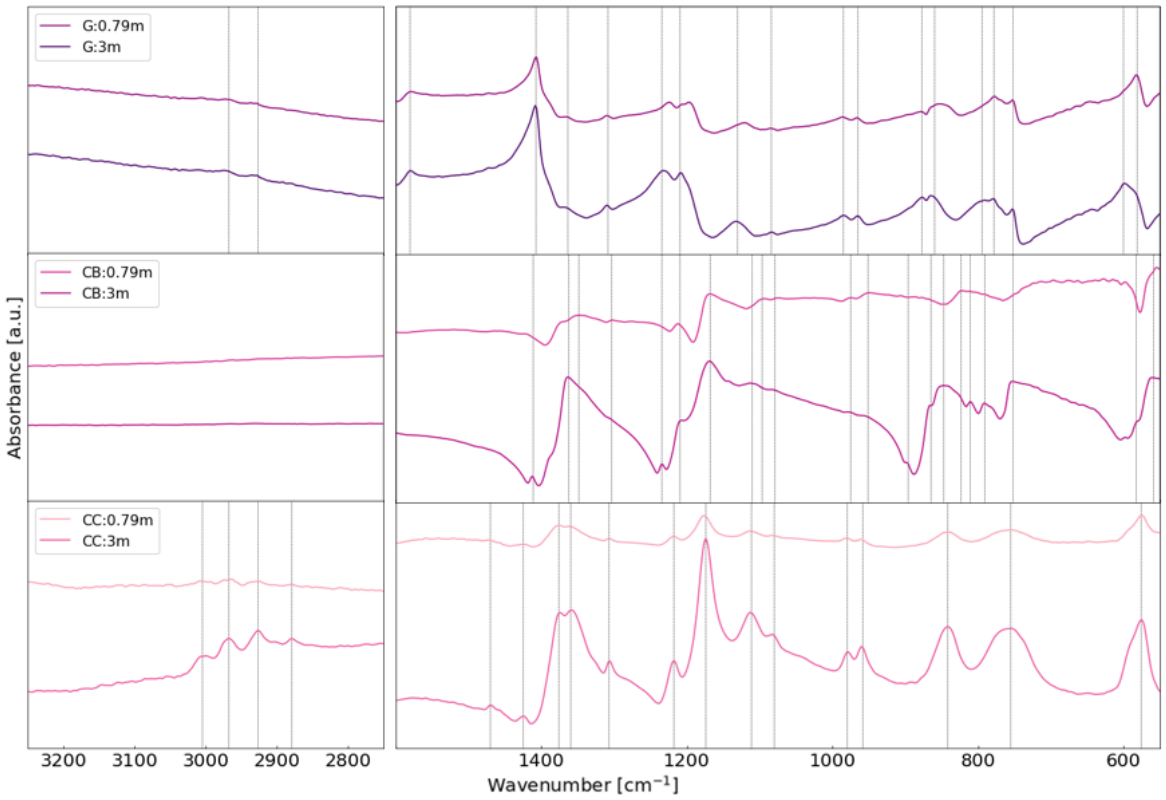

Figure 4.14: FTIR spectra for the cathodes, both at high wavenumbers between 2750 cm^{-1} and 3250 cm^{-1} and at low wavenumbers from 550 cm^{-1} to 1600 cm^{-1}. Note that the scale is different in the six panels.

4.1.5 X-ray diffraction analysis of graphite

The X-ray diffractograms of pristine graphite and G:0.79m:100cycles are found in Figure 4.15. The pristine sample has four peaks. Two at 26.6° and 54.7°, corresponding to the (002) and (004) plane of carbon, respectively. There are also peaks caused by aluminium. One at 65.1°, related to the (220) plane, and one at 78.3° which corresponds to the (311) plane. The d-spacing is then 3.35 Å, 1.68 Å, 1.43 Å and 1.22 Å for these peaks, from the lowest to the highest 2θ value. All peaks are very sharp, and the highest intensity is for the (002) carbon peak. There is barely any noise for this sample. The Scherrer equation (Equation 2.12) was used to calculate the average crystallite size of the graphite particles. It was found that the FWHM of the carbon (002) peak is 0.15°, corresponding to a crystallite size of 56.8 nm.

For the G:0.79m:100cycles, the same peaks are present, but their features have changed. Both aluminium peaks now have higher intensities, with the (220) peak being the highest. The positions of the aluminium peaks are the same as previously, and they are still very narrow. In addition, four small aluminium peaks at 38.5°, 44.7°, 112.0° and 116.0° have appeared. The (002) carbon peak has changed drastically after cycling. Its relative intensity is significantly reduced, and the peak is split in two. In addition,

a shoulder has appeared at the right side of the peak. The (004) carbon peak has also become wider. The highest part of the carbon (002) peak has the same position as for the pristine sample, but the other part of the split peak has a maximum at 25.9°, which corresponds to a d-spacing of 3.44 Å. The Scherrer equation was again used to estimate the average crystallite size for the two phases causing the different (002) peaks. It is assumed that the peaks are symmetrical for these calculations. The peak at 25.9° has an FWHM value of 1.2°, corresponding to an average crystallite size of 7.1 nm. The FWHM is 0.4° for the peak at 26.6°, indicating an average crystallite size of 21.3 nm.

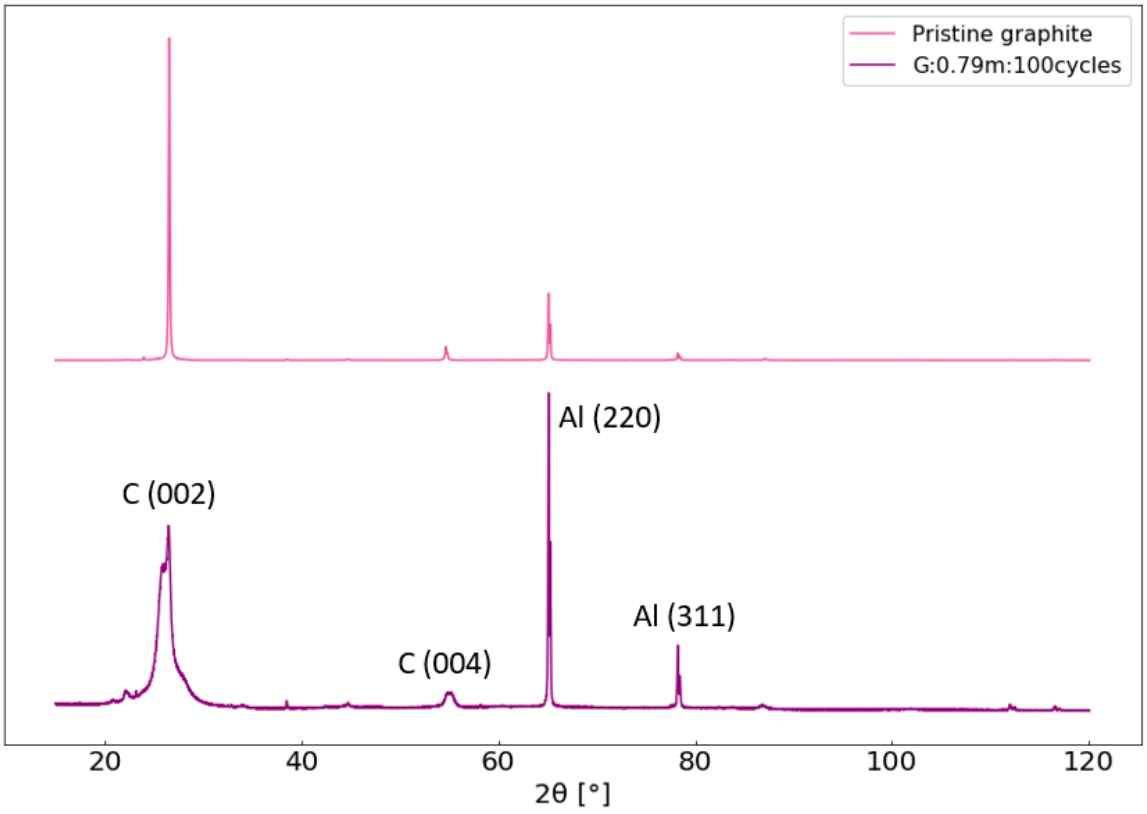

Figure 4.15: The X-ray diffractograms for the pristine graphite sample and G:0.79m:100cycles.

The results so far reveal less irreversible reactions occurring when using graphite than carbon black. Due to this advantage, graphite as conductive additive was selected for further studies in a LNMO cathode. The electrochemical characterisation of the cathode was performed with 0.79m LiFSI in $P_{111i4}FSI$ electrolyte, as 3m LiFSI in the electrolyte caused salt to precipitate. Additionally, the work conducted by my co-worker Mika Serna Malmer this semester [87], has shown that the cells with LNMO and carbon black in the cathode, and 0.79m LiFSI in $P_{111i4}FSI$ as the electrolyte, exhibit better capacity retention than the one with 3m LiFSI, and similar to the reference carbonate-based electrolyte with 1M $LiPF_6$. The coulombic efficiency was also better with 0.79m LiFSI in $P_{111i4}FSI$, compared to the carbonate-based electrolyte.

4.2 The LNMO:G:0.79m cell

4.2.1 Galvanostatic cycling

The cells with LNMO cathodes underwent galvanostatic cycling, where the two first cycles were with a C-rate of C/10, the next 50 cycles were at C/2, before ending it with two more cycles at C/10. In Figures 4.16 and 4.17, the discharge capacities and efficiencies of the LNMO cells are presented, respectively. The graphs are the average of three cells with the same configuration. For LNMO:ref, the capacity is relatively constant and only drops from 132.5 mAh/g to 131.0 mAh/g. At the lower rate, the capacity is reduced, 121 mAh/g and 124 mAh/g for the first two cycles, and 129 mAh/g for the last cycles. The discharge capacity of LNMO:G:0.79m show more variation between cycles, and the values are lower, ranging from 113.0 mAh/g to 120.0 mAh/g at C/2. Again, there is a reduction of discharge capacity over cycles, and the capacity drops more than for LNMO:ref. At C/10 the capacity is higher than at C/2, with values being 131 mAh/g and 130 mAh/g for the two first cycles, and 124 mAh/g for the last two cycles. The efficiency of LNMO:ref increases slightly throughout the cycling. For the first C/2 cycle, the efficiency is 95.0%, and for the last, it is 98.1%. LNMO:G:0.79m has similar efficiencies, with values between 94.0% and 99.8%. However, there is more variation between each cycle and no general trend as cycling progresses.

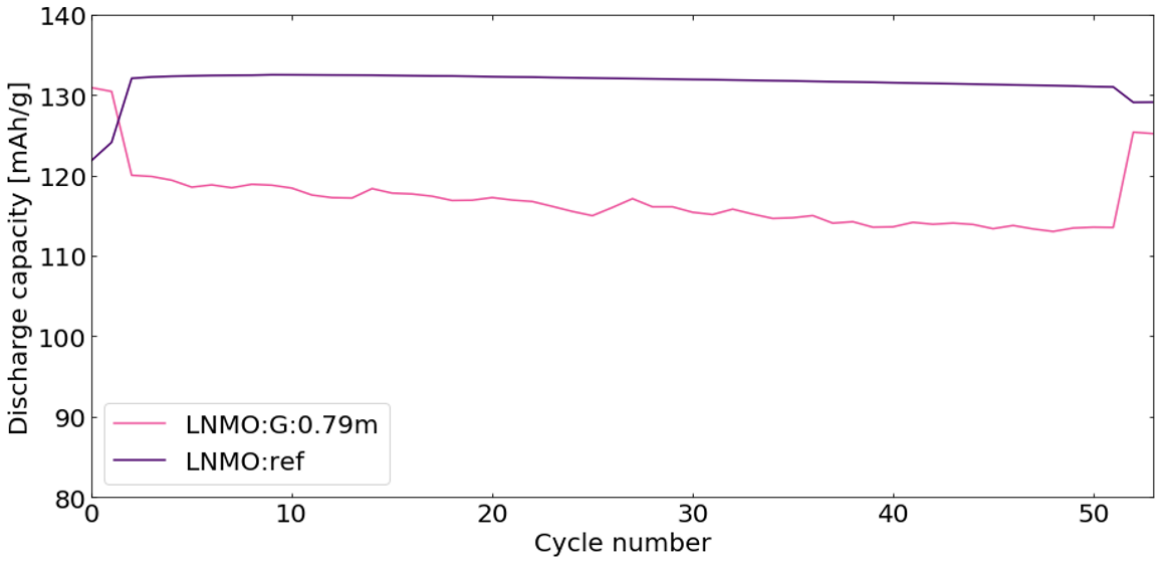

Figure 4.16: The discharge capacity of LNMO:ref and LMNO:G:0.79m. The first and last two cycles were with the C-rate C/10, and the 50 cycles between them were at C/2.

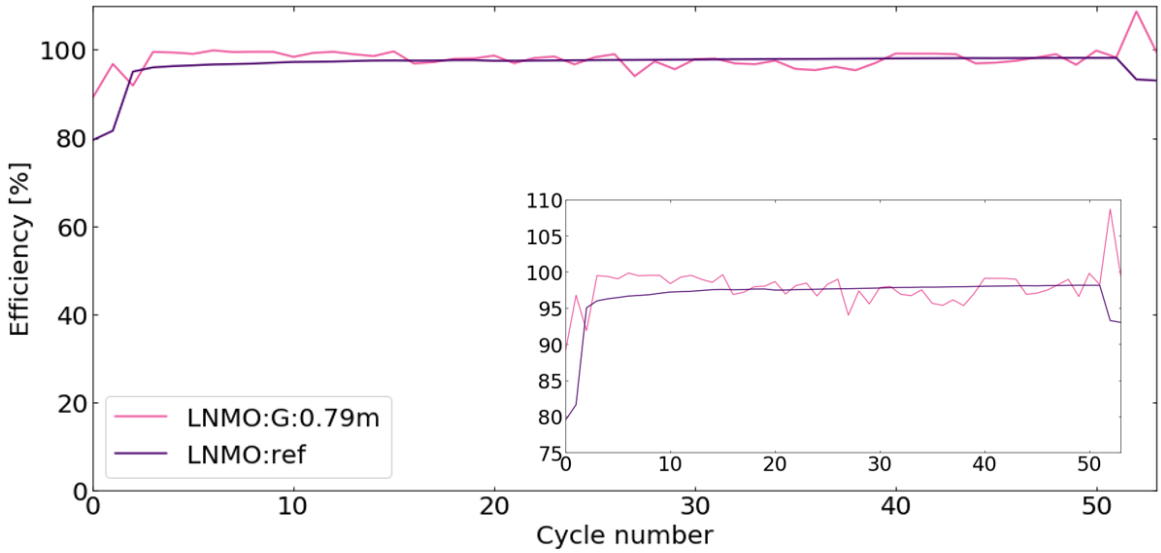

Figure 4.17: The efficiency of LNMO:ref and LNMO:G:0.79m. The first and last two cycles were with the C-rate C/10, and the 50 cycles between them were at C/2.

4.2.2 Scanning electron microscopy

SEM images of both pristine and cycled LNMO cathodes are seen in Figure 4.18. The first image, Figure 4.18a, is the pristine LNMO cathode with carbon black as conductive additive. The LNMO particles are spheres with triangular features, and between those, there is a network of carbon black nanoparticles and the binder. Figures 4.18b and 4.18c show the LNMO:ref cathode. No apparent change caused by the cycling is observed for these cathodes. The pristine LNMO cathode with graphite can

be seen in Figure 4.18d. The spherical LNMO particles and the graphite particles with sharp features are observed. After cycling (Figure 4.18e), the surface features of the cathode are more blurred, and it is more difficult to distinguish individual features. The graphite particles have softer edges due to a surface film. The LNMO particles are also partially covered, but some also inherit the same features as the pristine cathode.

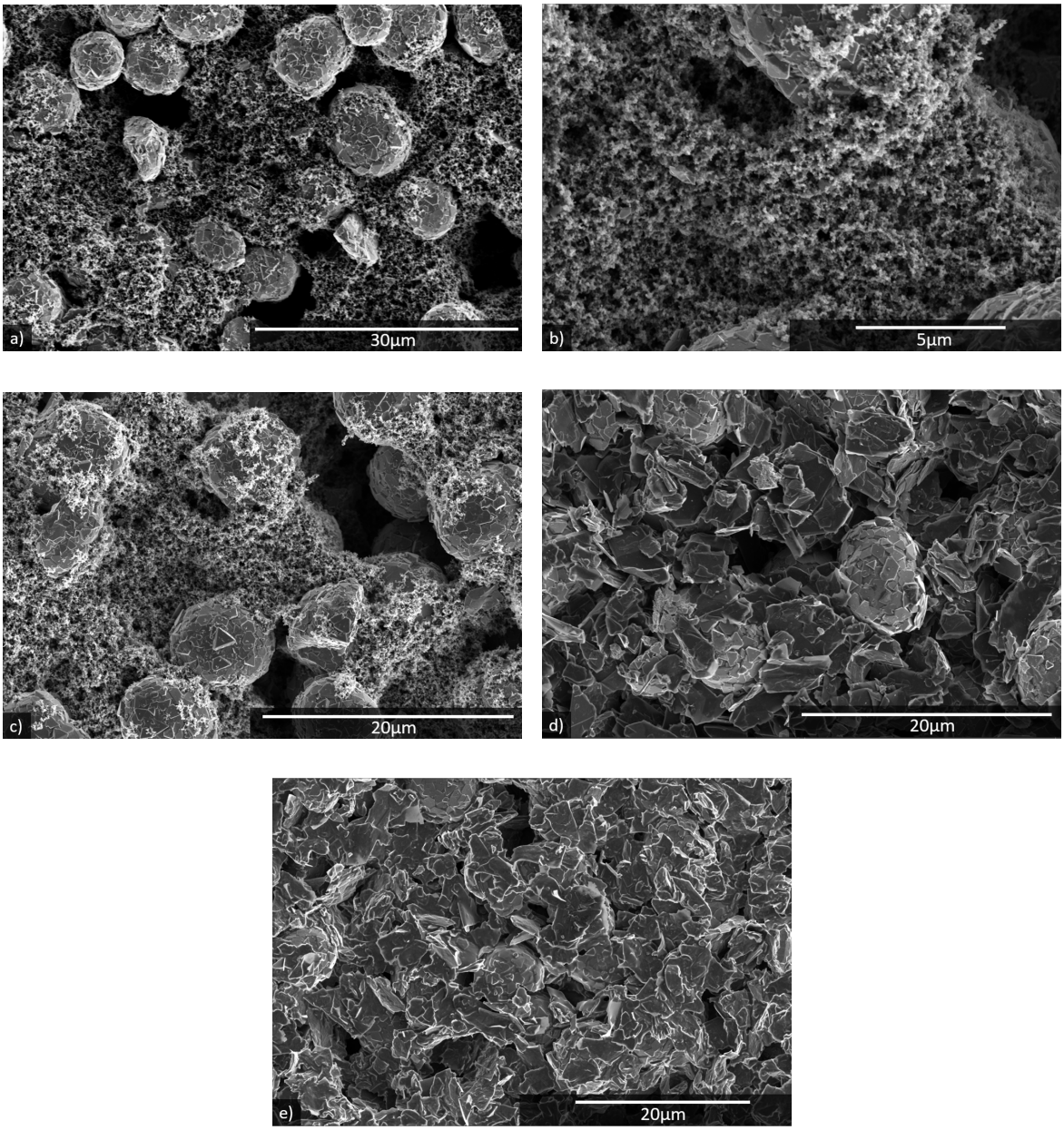

Figure 4.18: SEM images of a) the pristine LNMO cathode with carbon black, b,c) LNMO:ref, d) pristine LNMO cathode with graphite and e) LNMO:G:0.79m.

4.2.3 Energy dispersive X-ray spectroscopy

From the EDS maps of the LNMO:G:0.79m cathode in Figure 4.19, it can be observed that manganese, nickel and oxygen are primarily present at the LNMO particles, but there is some signal coming from the graphite too. This is also seen for the pristine cathode, shown in Figure C.2 in appendix C. The spectrum reveals that all elements, carbon, oxygen, manganese, nickel, phosphorous, fluorine, sulfur and nitrogen, are present at the surface. As seen for the carbon cathodes, there is less signal from the space between the particles. Nitrogen and fluorine are evenly distributed at LNMO and graphite, but it can be observed that there is more sulfur at the graphite than the LNMO particle. In addition, it appears that there is more phosphorous between the particles than at their surface. Cycling has increased the amount of oxygen at the graphite particles.

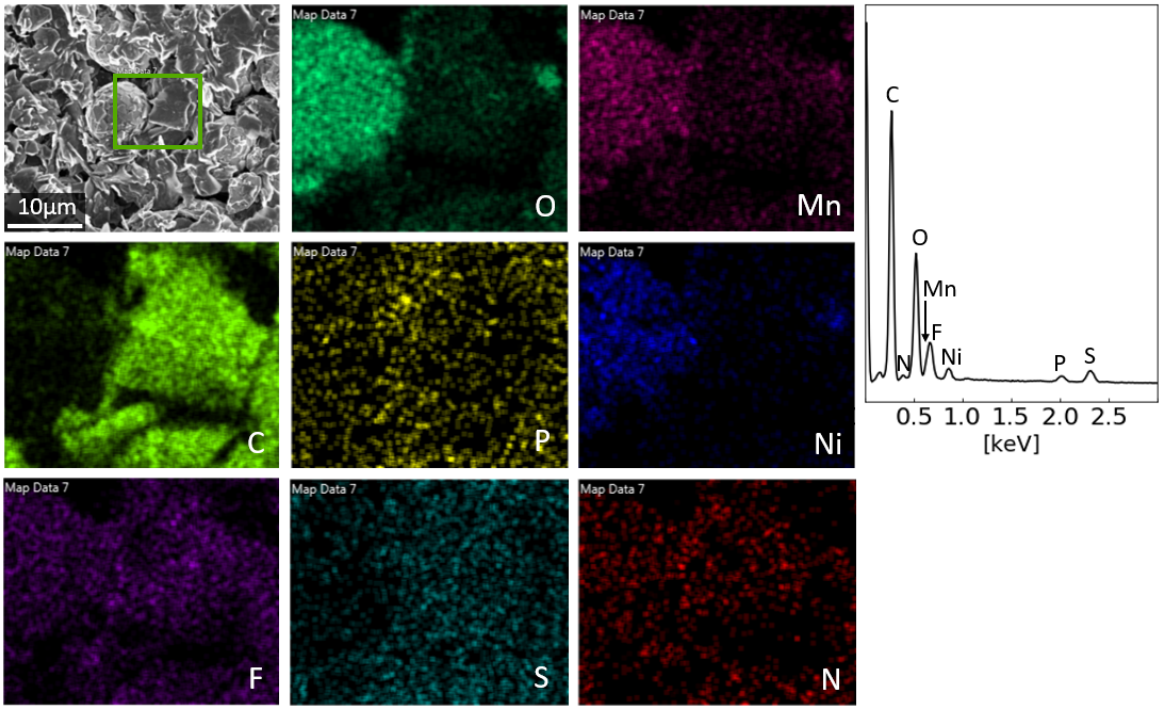

Figure 4.19: EDS maps and spectrum of LNMO:G:0.79m cathode. The green square in the SEM image indicates the area of the mapping.

Chapter 5

Discussion

5.1 Effect of CMC as the binder

In the initial phase of the work, experiments were conducted to decide whether CMC was an appropriate binder, as its response to high voltages was unknown. To test this, two graphite cathodes were cast. One with CMC and one with PVDF. These were used in G:0.79m cells, and cyclic voltammetry was performed. The main difference between the two is the onset potential. It is expected that the threshold potential is higher during the first cycle than the other cycles because of an initial kinetic hindrance related to increasing the distance between the graphene sheets [64]. This behaviour is observed when using CMC as the binder, where the onset potential is 4.58±0.01 V during the first cycle, and only 4.55±0.00 V during the other cycles. Others have observed similar behaviour with CMC [64][88][89][90]. When using PVDF, the threshold potential is 4.53 V for all cycles, which is lower than that of the cells with CMC. It cannot be explained why the onset potential is not higher during the first cycle as expected and observed by Qi *et al.* making carbon cathodes with PVDF [43]. Anyways, it is concluded that CMC is a suitable binder for cycling up to 5 V, due to this binder causing the cell to exhibit the best electrochemical behaviour. CMC is therefore used in the G:0.79m:100cycles, G:3m, CB:0.79m and CB:3m cathodes.

5.2 Reactions with the graphite cathode

Both oxidation and reduction reactions are observed, which indicate anion intercalation and deintercalation [64][88]. The reductions correspond solely to anion deintercalation, and the oxidations can be both anion intercalation and electrolyte oxidations. There are three oxidation and reduction peaks, implying that the intercalation and deinter-

calation occur in three stages in this potential range. More precisely, this means that anions are not intercalated in between all graphene sheets at once, but fill *e.g.* every fourth gap during the first stage, then every other gap, before all are filled during the last stage [66]. The similarities observed for G:0.79 and G:3m indicate that the same reactions happen. One difference is that G:0.79m cells experience more reactions than the G:3m cells, both oxidations and reductions. Another is that the three different stages of intercalation are less distinct for G:3m than G:0.79m. Both phenomena can be explained by the G:3m cell having a lower reaction rate. With the chosen scan rate, there is insufficient time to complete one intercalation stage before the next is initiated [72]. The limited reversibility of the reactions at approximately 60% indicates the presence of irreversible reactions. Some can be irreversible anion intercalation, but the SEM images in Figure 4.8 indicate that electrolyte oxidation reactions also occur. The reversibility is higher for the G:0.79m than the G:3m cells. However, whether this is due to the anion intercalation being more reversible or that a larger fraction of the reactions is electrolyte oxidations, is unknown. The onset potential of the G:0.79m cell is significantly lower than for the G:3m cell. This behaviour can be caused by a kinetic factor, increasing the activation energy of interfacial anion transfer [62].

The cumulative charge of the various cells provides information about the amount of irreversible reactions occurring. Higher values correspond to more irreversible reactions taking place. The values for G:0.79m and G:3m are 282.2 C/g and 232.1 C/g, respectively. Significant variations between the individual cells contribute to much uncertainty. The irreversible reactions can be both irreversible anion intercalation and electrolyte oxidations, and it can therefore not be determined how much of the cumulative charge is attributed to the anion decomposition.

After cycling, salt crystals were present in the G:3m cell. Since the salt was found throughout the cell, not only at the cathode, it must be precipitation of LiFSI salt and not insoluble salt products formed from electrolyte decomposition. From Figure 4.8d, indentations in the graphite surface can be observed. As these were not present before cycling, and it was only observed for the G:3m cathodes, the damage must be from the precipitated salt. This damage and the salt precipitation indicate that the combination of graphite and the electrolyte containing 3m LiFSI is inappropriate. There is an excessive amount of Li-salt, and all the Li^+ ions cannot be utilised.

Cyclic voltammetry with 100 cycles was carried out to see if the anion intercalation has a negative impact on the graphite particle structure. This voltammogram has a different appearance than the G:0.79m and G:3m cells, due to the difference in scan rate [72], which was 0.1 mV/s for the cells cycled five times and 1 mV/s for the ones

cycled 100 times. The intercalation stages are then less distinct. The first few cycles have poorer behaviour than the rest but after that, the behaviour of the cell is relatively constant for all cycles. This is seen from the shape of the graph, and because average reversibility is 76.2% during the 10th cycle, and 77.8% during the 100th cycle, with a gradual increase between them. This demonstrates that the total amount of oxidation reactions do not increase with cycle number, as expected if the continuous intercalation and deintercalation degrade the graphite structure [62].

Post mortem characterisation of the cells conveys differently. The SEM images reveal that rougher particles are present after cycling, and these appear to be degraded graphite particles. The XRD results also support this. After cycling, the relative intensities of the aluminium peaks were much higher than before. Four new peaks corresponding to aluminium were also observed. This indicates non-uniform coverage of the cathode caused by graphite degradation, causing more interactions with the aluminium foil underneath. The splitting and widening of the (002) carbon peak provide additional information. This peak corresponds to the interplanar distance of the graphene sheets, and the splitting indicates that some of the graphite now has an increased spacing between the planes. The new d-spacing of 3.44 Å indicates that some of the graphite has transformed into turbostratic carbon. The crystallite size for this phase is 7.1 nm, much lower than 56.8 nm which was calculated for the pristine graphite. Both these observations are evidence that the anion intercalation has degraded some of the graphite. There is still a peak corresponding to a d-spacing of 3.35 Å, indicating that parts of the graphite have not been exposed to intercalation. Still, it has broadened compared to the peak of the pristine graphite, with the average crystallite size being reduced to 21.3 nm. The two co-existing phases show that some of the graphite is severely degraded from the intercalation, while other parts are less affected. A possible explanation for the broadening of the (002) peak is that parts of a crystallite are exposed to intercalation while others are not. However, what was previously one crystallite is now split into multiple ones, where some have a d-spacing of 3.35 Å, and others 3.44 Å. Therefore, the size of all crystallites is reduced. What is not considered when calculating the crystallite sizes is other characteristics that can affect the peak broadening *e.g.* lattice strain. If there are still anions in the structure causing inhomogeneous strain, that will also contribute to peak broadening. A shoulder is seen at the right side of the carbon (002) peak, and its origin is not known. Electrochemical testing and *post mortem* characterisation of G:0.79m:100cyles have proved that the anion intercalation occurring when cycling to 5 V cause structural changes to the graphite particles. This is observed both by changes in interplanar distance between graphene sheets and by the morphology of some particles at the microscale.

Since the salts are the only components of the electrolyte, the electrolyte oxidations occurring must be salt decomposition, and the film is created through these reactions. At both the G:0.79m and G:3m cathodes, the film presents a similar appearance, covering the particles and diminishing their sharp features. The EDS and FTIR analyses provide information about the film composition. Carbon is primarily due to the graphite particles, but the P^+_{111i4} cation also contains carbon atoms, and if there is any residue of DMC used to rinse the cathodes, the carbon can also be from this. Oxygen can be from the anion, adsorbed species at the pristine surface, DMC or reactions with air when moving the samples for EDS analysis. Phosphorous is from the P^+_{111i4} cation, and nitrogen, fluorine, and sulfur are from the anion.

The G:0.79m and G:3m cathodes have comparable features, with similar amounts of the various elements distributed across the particles. The lighter elements, carbon, oxygen, fluorine and nitrogen, show little or no signal from the space between particles. This is because the X-rays sent from those atoms in these areas do not have enough energy to escape and reach the detector. This is not an issue for the heavier elements that create X-rays with higher energies [91]. The weight percentages given for the different elements are not studied in detail due to uncertainties related to these values. However, the presence of the element and a rough estimation of the amounts can be decided.

For both samples, carbon is the dominating element. However, other elements are also present at the surface after cycling. The presence of phosphorous at both cathodes indicates that residues of the IL are at the surface, as oxidation of the cation will not happen [92]. Sulfur, fluorine and nitrogen can come from residues of the electrolyte not being adequately rinsed off the surface or from chemical compounds formed during anion decomposition. Oxygen can have many origins, but the increased amount after cycling indicates that some originate from the FSI^- anion, reactions with the anion, or possibly DMC used for rinsing the cathodes.

The features of EDS data for the G:0.79m:100cycles cathode differ from that of the other graphite cathodes. The weight percent of carbon has significantly decreased, and that of oxygen has increased. It is logical that the rougher particles exhibit a higher oxygen and sulfur concentration than the other particles. They have been severely degraded, which has caused the surface reactions with the electrolyte to primarily occur at them instead of the less degraded particles. This data also support what Lee *et al.* [70] observed, a film made of $S = O$. They also observed $Li - F$ species, which cannot be determined to be present at the G:0.79m:100cycles cathodes due to fluorine being evenly distributed across the surface, indicating that it can also be from

electrolyte residues. However, their use of PVDF as the binder can also have affected the reactions occurring, as it contains fluorine. Kotronia *et al.* [67] studied cycled graphite cathodes and observed differently. They found no significant film formation when using 1M LiFSI in $Pyr_{14}FSI$, even though they cycled to 5.1 V. This variation in the behaviour is unexpected, as the surface reactions are anion decomposition, and the anion is the same. It might be the differences in the cell configuration, different IL and graphite, that cause this deviation. It is worth noting that the voltammogram does not show an increase in the overall amount of oxidations, but the EDS maps indicate that there are more reactions happening at degraded particles, which means that the amount of surface reactions should increase with time, as more graphite degradation occurs.

FTIR provide additional information about the surface film. As the pristine cathodes are used as background, the binder should not affect the results. The absorbance depends on many factors, one being the pressure applied to the sample during the measurements. It is, therefore, difficult to compare values for different samples. Still, it is appropriate to compare the following absorbances: G:0.79m to G:3m, CB:0.79m to CB:3m, and CC:0.79m to CC:3m. This is because these comparable samples were analysed during the same session, keeping the pressure stable for the samples. In addition, three parallel analyses of each sample gave graphs with similar absorbance values, indicating the reliability of the results.

Before discussing the FTIR spectra for the graphite cathodes, the FTIR spectra of the CC:0.79m and CC:3m cells deserve attention. These two spectra are similar to each other, the main difference being the peak intensities. Girard [85, p. 174] performed FTIR measurements on neat $P_{111i4}FSI$ IL. Comparing his obtained spectrum with the spectra of CC:0.79m and CC:3m, a remarkable similarity is observed. The same peaks are seen, and their relative intensities are comparable. The film at the surface of these cathodes is therefore found to primarily be IL residues, not electrolyte decomposition products.

The FTIR spectra of the G:0.79m and G:3m cathodes reveal that organic species are present. These can originate from either the P^+_{111i4} cation or the DMC used to rinse the samples after cycling if it has not evaporated fully. The observed OCO stretching indicates that some DMC is still present at the surface, and this means that the observed peaks corresponding to vibrational modes of CH_3 have two possible origins, the cation and DMC. However, the torsion and stretching of CH_2 that are visible for the graphite cathodes are inherent to the cation. This corresponds well to the observation of phosphorous in the EDS maps. There are also peaks caused by

either the anion itself or decomposition products made from the anion. The detected SNS and SO_2 bonds are inherent to this. In addition, some peaks can be from the $SO_2 - N - SO_2$ and SF stretching, but this cannot be confirmed due to overlapping frequencies for vibrational modes of other chemical bonds. One of the peaks, at 877 cm^{-1} could be from Li_2CO_3 bending, but this substance also has a characteristic peak around 1450 cm^{-1} which is not observed. Therefore, it is determined that Li_2CO_3 is not present.

The graphite cathodes have FTIR absorbance spectra that differ significantly from those of the C-coated Al cathodes. Due to this, it is known that the film at these surfaces is more than just electrolyte residue. Electrolyte decomposition reactions have contributed to making the film, changing the environment to something other than the electrolyte itself, and therefore affecting the presence of peaks and their relative intensities. In addition, the cathodes have traces of the cation, indicating IL residues. It can therefore be concluded that there are both electrolyte residues and decomposition products at the surface.

An observation for all types of cathodes, both graphite, carbon black and C-coated Al, is that 3m LiFSI in the electrolyte consistently causes more absorbance than 0.79m LiFSI, indicating more of the film at the surface. Since the electrochemical data do not indicate a significant difference in electrolyte oxidation reactions depending on the chosen electrolyte, it appears this is due to more electrolyte residues at the cathodes cycled with the 3m LiFSI electrolyte. It is possible that the increased viscosity of the 3m LiFSI electrolyte, compared to the other, has caused the rinsing of the cathodes to be less effective.

5.3 Reactions with the carbon black cathode

The voltammograms for CB:0.79m and CB:3m show that there are primarily oxidations happening at these cathodes. Since salts are the only components of the electrolyte, and cations do not oxidise, these irreversible reactions must be FSI^- anion oxidation [92]. A small negative current when reducing the voltage is the only indication of a reduction occurring. But as these small peaks are at the same place as the reduction peaks for C-coated Al, it is understood that these are anion deintercalation. The small current fluctuations observed upon increasing the voltage are anion intercalation. The loading of the carbon black cathodes is low, with the weight of carbon black on the cathode being approximately five times the weight of the carbon coating. These fluctuations, which are much smaller for the CB:0.79m and CB:3m cells than the

CC:0.79m and CC:3m cells, might therefore be from reactions with the coating, not the carbon black.

The average cumulative charge for CB:0.79m and CB:3m is 558.8 C/g and 578.0 C/g, respectively. No correlation between the concentration of Li salt and the cumulative charge was found, due to the average value being higher for G:0.79m than G:3m but lower for CB:0.79m than CB:3m, and the significant variations between individual cells. However, the cumulative charge is much higher for the cells with carbon black cathodes than the ones with graphite cathodes. This shows that during 5 cycles, more irreversible reactions occur with carbon black than with graphite, hence there is more electrolyte decomposition.

One similarity with the graphite cells is that the onset potential is higher when using the electrolyte with 3m LiFSI than when using the one with 0.79m LiFSI. However, the confidence intervals overlap for the two carbon black cells, indicating that this difference can be random. The CC:3m cathodes also cause a higher onset potential than the CC:0.79m cathodes, but the uncertainty is even bigger than for the cells with carbon black cathodes. It can therefore not be concluded that a higher concentration of LiFSI in the IL increases the onset potential, even if the average values are higher with 3m LiFSI than 0.79m LiFSI for all cathodes. Another similarity is that salt was precipitated when using the electrolyte with 3m LiFSI. No damage to the CB:3m cathodes was observed, unlike for the G:3m cathode. This can be because the small size of the carbon black particles makes the cathode denser and more mechanically stable. The cathode is also very thin, limiting the possibility of making indentations on the surface. Even though the cathode is not damaged, salt precipitation should be avoided, as it traps the Li^+ ions.

EDS analysis of the CB:0.79m and CB:3m cathodes reveals interesting information. First, the percent of carbon is much higher for CB:0.79m than the other, indicating less film formation at this cathode. In the SEM images, the film is more visible for the CB:0.79m cathode, but the EDS results prove that there is also a film at the CB:3m cathode. It might also be that some of the electrolyte decomposition products have been integrated into the particle surfaces, as observed by Younesi *et al.* [68]. The presence of phosphorous shows that there are still electrolyte residues left, as this comes from the cation. Fluorine, sulfur and nitrogen are evidence that the anion or its decomposition products are also present.

The FTIR spectra of CB:0.79m and CB:3m reveal no indication that DMC is still present from the rinsing. The only peak that can only be ascribed to the cation is the torsion of CH_2, and this is only found for the CB:0.79m cathode. However, this information and the EDS data showing phosphorous prove that the cation is present at the surface. Vibrations caused by SF bonds, SNS bonds and SO_2 are also observed, and these are from the FSI^- anion. CB:0.79m also has a peak that was found to be from $SO_2 - N - SO_2$ stretching, substantiating the presence of anions or products formed from anion decomposition. Comparing these spectra to those of CC:0.79m and CC:3m, the dissimilarity is obvious. The peaks present for both are found at different absorbances for the two types of cathodes, their relative intensities differ, and the presence of specific peaks is also different. This indicates that there has been film formation at the cathodes, changing the environment compared to that of the C-coated Al where it is found to be primarily IL residues. As for the graphite cathodes, this is due to electrolyte decomposition creating a film. Including the information that the cation is also at the surface, it is understood that both electrolyte residues and a film formed from oxidation reactions cover the surface. The FTIR spectra of the graphite cathodes and those of the carbon black cathodes also differ significantly, revealing that the type of carbon affects the electrolyte degradation reactions.

5.4 The LNMO:G:0.79m cathode

The LNMO:ref cell has a good rate performance. It is observed that the discharge capacity is higher at C/2 than C/10, which is unexpected [32][93]. To understand why this happens, further analyses would be needed. The LNMO:G:0.79m cell has a significantly lower discharge capacity than the LNMO:ref cell at a C-rate of C/2. The IL-based electrolyte has been shown to slightly reduce the discharge capacity, but the large difference observed here is not expected to occur from the use of the electrolyte [87]. This suggests that the use of graphite is what reduces the capacity. It appears that the conductive network of the graphite particles is inferior for LNMO:G:0.79m, reducing the electronic conductivity of the cathode [94]. With less contact between conductive carbon and the LNMO particles, the capacity can only partially be exploited. There can be multiple reasons for the slow decline in discharge capacity. One is Mn dissolution, causing structural instability of LNMO. Irreversible electrolyte oxidations forming a surface film can also contribute to this negative evolution. Another feature of the LNMO:G:0.79m discharge capacity curve is the variation of the values between each cycle, which is not observed for the reference cell. This happens because there is anion intercalation into the graphite particles, contributing to the capacity

[88], and this intercalation varies more from cycle to cycle than the Li^+ intercalation into LNMO.

The anion intercalation also has the same effect on the efficiency, which varies between cycles. These values are comparable to those of the reference cell. Still, it is not known what the efficiency of the Li^+ intercalation into LNMO is and what can be attributed to the anion intercalation. IL-based electrolytes have been found to increase the efficiency of cells [93], though the effect of the IL can not be discerned from that of graphite based on these results.

Despite observing signs of anion intercalation, the SEM images do not indicate any alteration in the graphite structure, similar to what was observed in the G:0.79m:100cycles cells. However, this is not surprising given that the LNMO:G:0.79m cells had a lower cut-off voltage of 4.85 V and underwent fewer cycles. Furthermore, the remaining graphite cathodes also did not exhibit any visible degradation, suggesting further cycling could cause enough anion intercalation to affect the structure eventually.

The SEM images reveal a film at the LNMO:G:0.79m cathode surface. While the graphite is completely covered, the LNMO particles only have partial coverage. This can indicate that reactions happen more at the carbon than the active material, in line with the findings of Carroll *et al.* [71]. The EDS analysis provides more information about the film. The spectrum reveals that all the elements from the electrolyte are present. Since fluorine and carbon are also present in the binder, the map for these elements can not be used to get information about the film. The presence of nitrogen proves that the anion or its decomposition products are present, but it is evenly distributed across the surface and therefore does not provide further information. More oxygen is observed at the carbon, compared to the situation before cycling. This must be from the FSI^- anion or DMC. The signal for sulfur is larger from the graphite than the LNMO particles, substantiating that reactions occur more at the conductive carbon than the active material. It is also in line with the findings of Lee *et al.* [70] that S = O species are found in the film when cycling cells with IL-based LiFSI electrolytes. Since the reactions are unevenly distributed at the surface, it indicates that the decomposition is electrochemical, not thermal, as Yang *et al.* [69] found after cycling of LNMO cathodes with $LiPF_6$-based electrolyte. This is in line with LiFSI having better thermal stability. As previously mentioned, the phosphorous is from residues of the electrolyte not being properly removed during washing. This matches the results that there is more phosphorous between the particles, where the rinsing would be less effective than at the surface. Li *et al.* [12] observed a mutual exchange of surface species between the conductive carbon and active material. That is not

observed in this work. If the amount of manganese or nickel present at the graphite particles increased during cycling, it would indicate such a communication. However, since both elements were present at the surface both before and after cycling and no apparent change is observed, no conclusion can be drawn from this.

Chapter 6

Conclusion

The reactions occurring at graphite and carbon black during cycling between 3 V and 5 V have been investigated. The electrolytes used were 3m and 0.79m LiFSI in the IL $P_{111i4}FSI$. Interesting findings appeared through cyclic voltammetry measurements, SEM, EDS, FTIR and XRD analysis. It is found that both anion intercalation and film formation through electrolyte degradation occur at the graphite cathodes. The intercalation causes severe irreversible graphite degradations, and the degraded particles become sites for increased amounts of electrolyte oxidations. With carbon black cathodes, the reactions are primarily surface reactions, with only minor fluctuations in the voltammograms indicating some reversible intercalation. The surface reactions form a film similar to that created on the graphite cathodes, though FTIR proves that the chemical environment differs depending on the cathode used. Both anion species and cation species were observed from EDS analysis. The presence of the cation indicates that electrolyte residues are still present at the surface, and the anion species is either from the residue or decomposition products. However, results prove that there are decomposition products, too, not only residues. The film of the decomposition products is shown to contain sulfur and oxygen. Still, based on the results, it can not be said if observed nitrogen and fluorine are inherent to the film or only from electrolyte residues. Overall, it is found that there are less irreversible reactions with graphite than with carbon black, but graphite degradation is a severe problem that causes further electrolyte oxidation.

Among the two electrolytes compared, the one containing 0.79m LiFSI proved superior due to LiFSI salt precipitation observed after cycling with the 3m LiFSI electrolyte. Although the film exhibits similar characteristics, more chemical species are present on the surface after cycling with the 3m LiFSI electrolyte, which can be attributed to

an increased amount of electrolyte residues. While the onset potential for reactions is improved with the 3m LiFSI electrolyte, and there is reduced anion intercalation into the graphite, the issue of salt precipitation stands out as more significant.

Cells with LNMO, graphite as the conductive additive, and the electrolyte with 0.79m LiFSI were made, and they underwent galvanostatic cycling before the cathodes were characterised with SEM and EDS. The results indicate that the electronic conductivity network is insufficient, resulting in a lower discharge capacity than observed for the reference cell. Anion intercalation into graphite is observed through relatively large variations in the discharge capacity and efficiency between each cycle. Except for these fluctuations, the efficiency values are similar to the reference cell's. After cycling, the surface is covered in a film, and for these cathodes it is also observed that it consists of sulfur and oxygen, with a possibility of nitrogen and fluorine being a part of the film too. Additionally, it appears that more reactions occur at the graphite than the active material.

Chapter 7

Further work

Even though there have been multiple intersting findings in this work, there is still room for improvement and further investigations.

For the G:0.79m:100cycles cathodes, structural degradation and an increased amount of surface reactions at the severely degraded particles are observed. However, there is no indication in the voltammogram that the total amount of surface reactions increase with further cycling, as expected from the theory. Longer cycling with the graphite cathodes could reveal if this will change over time. If there is no indication that the total amount of surface reactions increased from the cycling, an effort should be put into understanding why it remains constant.

Different electrolytes should also be tested, to see if they reduce the amount of unwanted reactions. As previously mentioned, both the use of certain ILs and the use of some solvents can hinder anion intercalation. It would be necessary to do further testing with the electrolytes, besides analysing the intercalation. Altering the system will also affect properties like efficiency and capacity, so this must also be studied.

In this work, cells with an LNMO cathode containing graphite together with IL-based electrolytes have been tested, and my co-worker Malmer [87] has tested cells with LNMO cathodes containing carbon black together with the IL-based electrolytes. It would also be interesting to make cells with an LNMO cathode with graphite together with the $LiPF_6$-based electrolyte. Galvanostatic cycling of such a cell would make it easier to distinguish the effect of the electrolyte and the conductive additive. The reactions happening at the cathode are complex, meaning that observed properties of the cell might not be solely due to one cell component, but can be inherent to specific combinations of electrolyte and conductive carbon.

It is found that graphite reduces the amount of electrolyte oxidation relative to using carbon black, but also causes poor electronic conductivity in the cathode. Carbon black does, on the other hand, provide a proper conductive network. Therefore, experiments with a combination of both carbons should also be carried out. Testing other types of conductive carbon additives can also be done since there is a vast variety of alternatives available, and they might show significantly different behaviours.

Bibliography

[1] W. Katzenstein and J. Apt, "The cost of wind power variability," *Energy Policy*, vol. 51, pp. 233–243, 2012, Renewable Energy in China.

[2] C. A. Hill, M. C. Such, D. Chen, J. Gonzalez, and W. M. Grady, "Battery Energy Storage for Enabling Integration of Distributed Solar Power Generation," *IEEE Transactions on Smart Grid*, vol. 3, no. 2, pp. 850–857, 2012.

[3] D. Rimpas, S. D. Kaminaris, I. Aldarraji, *et al.*, "Energy management and storage systems on electric vehicles: A comprehensive review," *Materials Today: Proceedings*, vol. 61, pp. 813–819, 2022, International Conference on Recent Advances in Mechanical Engineering and Nanomaterials.

[4] N. Nitta, F. Wu, J. T. Lee, and G. Yushin, "Li-ion battery materials: present and future," *Materials Today*, vol. 18, no. 5, pp. 252–264, 2015.

[5] Y. Chen, Y. Kang, Y. Zhao, *et al.*, "A review of lithium-ion battery safety concerns: The issues, strategies, and testing standards," *Journal of Energy Chemistry*, vol. 59, pp. 83–99, 2021.

[6] Y. Liu, R. Zhang, J. Wang, and Y. Wang, "Current and future lithium-ion battery manufacturing," *iScience*, vol. 24, no. 4, 2021.

[7] C. Julien, A. Mauger, A. Vijh, and K. Zaghib, *Lithium Batteries: Science and Technology*. Springer International, 2016.

[8] G. Liang, V. K. Peterson, K. W. See, Z. Guo, and W. K. Pang, "Developing high-voltage spinel lini0.5mn1.5o4 cathodes for high-energy-density lithium-ion batteries: Current achievements and future prospects," *J. Mater. Chem. A*, vol. 8, pp. 15 373–15 398, 31 2020.

[9] H. Zhao, W.-Y. A. Lam, L. Sheng, *et al.*, "Cobalt-free cathode materials: Families and their prospects," *Advanced Energy Materials*, vol. 12, no. 16, p. 2 103 894, 2022.

[10] C. M. Julien and A. Mauger, "Review of 5-v electrodes for li-ion batteries: Status and trends," *Ionics*, vol. 19, no. 7, pp. 951–988, Jul. 1, 2013.

[11] S. Ko, Y. Yamada, L. Lander, and A. Yamada, "Stability of conductive carbon additives in 5 v-class li-ion batteries," *Carbon*, vol. 158, pp. 766–771, 2020.

[12] W. Li, A. Dolocan, P. Oh, *et al.*, "Dynamic behaviour of interphases and its implication on high-energy-density cathode materials in lithium-ion batteries," *Nature Communications*, vol. 8, no. 1, p. 14 589, Apr. 26, 2017.

[13] P. Zheng, J. Sun, H. Liu, *et al.*, "Microstructure engineered silicon alloy anodes for lithium-ion batteries: Advances and challenges," *Batteries & Supercaps*, vol. 6, no. 1, e202200481, 2023.

[14] H. D. Yoo, E. Markevich, G. Salitra, D. Sharon, and D. Aurbach, "On the challenge of developing advanced technologies for electrochemical energy storage and conversion," *Materials Today*, vol. 17, no. 3, pp. 110–121, 2014.

[15] F. Wu and G. Yushin, "Conversion cathodes for rechargeable lithium and lithium-ion batteries," *Energy Environ. Sci.*, vol. 10, pp. 435–459, 2 2017.

[16] J. B. Goodenough and K. S. Park, "The li-ion rechargeable battery: A perspective," *Journal of the American Chemical Society*, vol. 135, pp. 1167–1176, 4 Jan. 2013.

[17] D. Werner, S. Paarmann, and T. Wetzel, "Calendar aging of li-ion cells— experimental investigation and empirical correlation," *Batteries*, vol. 7, 2 Jun. 2021.

[18] K. Xu, "Nonaqueous liquid electrolytes for lithium-based rechargeable batteries," *Chemical Reviews*, vol. 104, pp. 4303–4417, 10 Oct. 2004.

[19] R. Younesi, G. M. Veith, P. Johansson, K. Edström, and T. Vegge, "Lithium salts for advanced lithium batteries: Li–metal, li–o2, and li–s," *Energy Environ. Sci.*, vol. 8, pp. 1905–1922, 7 2015.

[20] Sungjemmenla, V. S. K., C. B. Soni, V. Kumar, and Z. W. Seh, "Understanding the cathode–electrolyte interphase in lithium-ion batteries," *Energy Technology*, vol. 10, no. 9, p. 2 200 421, 2022.

[21] C. L. Campion, W. Li, and B. L. Lucht, "Thermal decomposition of lipf6-based electrolytes for lithium-ion batteries," *Journal of The Electrochemical Society*, vol. 152, no. 12, A2327, Oct. 2005.

[22] H. H. Lee, C. C. Wan, and Y. Y. Wang, "Thermal stability of the solid electrolyte interface on carbon electrodes of lithium batteries," *Journal of The Electrochemical Society*, vol. 151, no. 4, A542, Feb. 2004.

[23] J. Y. Han and S. Jung, "Thermal stability and the effect of water on hydrogen fluoride generation in lithium-ion battery electrolytes containing lipf6," *Batteries*, vol. 8, no. 7, 2022.

[24] M. Liu, J. Vatamanu, X. Chen, L. Xing, K. Xu, and W. Li, "Hydrolysis of lipf6-containing electrolyte at high voltage," *ACS Energy Letters*, vol. 6, no. 6, pp. 2096–2102, 2021.

[25] Y. Yamada, C. H. Chiang, K. Sodeyama, J. Wang, Y. Tateyama, and A. Yamada, "Corrosion prevention mechanism of aluminum metal in superconcentrated electrolytes," *ChemElectroChem*, vol. 2, no. 11, pp. 1687–1694, 2015.

[26] H. B. Han, S. S. Zhou, D. J. Zhang, *et al.*, "Lithium bis(fluorosulfonyl)imide (lifsi) as conducting salt for nonaqueous liquid electrolytes for lithium-ion batteries: Physicochemical and electrochemical properties," *Journal of Power Sources*, vol. 196, pp. 3623–3632, 7 Apr. 2011.

[27] K. Zaghib, P. Charest, A. Guerfi, J. Shim, M. Perrier, and K. Striebel, "Safe li-ion polymer batteries for hev applications," *Journal of Power Sources*, vol. 134, no. 1, pp. 124–129, 2004.

[28] G. Yan, X. Li, Z. Wang, H. Guo, W. Peng, and Q. Hu, "Lithium difluoro(oxalato)-borate as an additive to suppress the aluminum corrosion in lithium bis(fluorosulfony)imide-based nonaqueous carbonate electrolyte," *Journal of Solid State Electrochemistry*, vol. 20, pp. 507–516, 2 Feb. 2016.

[29] Z. Lei, B. Chen, Y.-M. Koo, and D. R. MacFarlane, "Introduction: Ionic liquids," *Chemical Reviews*, vol. 117, no. 10, pp. 6633–6635, 2017.

[30] T. Yim, M.-S. Kwon, J. Mun, and K. T. Lee, "Room temperature ionic liquid-based electrolytes as an alternative to carbonate-based electrolytes," *Israel Journal of Chemistry*, vol. 55, no. 5, pp. 586–598, 2015.

[31] H. Niu, L. Wang, P. Guan, *et al.*, "Recent advances in application of ionic liquids in electrolyte of lithium ion batteries," *Journal of Energy Storage*, vol. 40, p. 102 659, 2021.

[32] D. T. Rogstad, M.-A. Einarsrud, and A. M. Svensson, "Evaluation of selected ionic liquids as electrolytes for silicon anodes in li-ion batteries," *Journal of The Electrochemical Society*, vol. 168, no. 11, p. 110 506, Nov. 2021.

[33] D. T. Rogstad, M.-A. Einarsrud, and A. M. Svensson, "High-temperature performance of selected ionic liquids as electrolytes for silicon anodes in li-ion batteries," *Journal of The Electrochemical Society*, vol. 169, no. 11, p. 110 531, Nov. 2022.

[34] R.-S. Kühnel, M. Lübke, M. Winter, S. Passerini, and A. Balducci, "Suppression of aluminum current collector corrosion in ionic liquid containing electrolytes," *Journal of Power Sources*, vol. 214, pp. 178–184, 2012.

[35] A. Balducci, "Ionic liquids in lithium-ion batteries," *Topics in Current Chemistry*, vol. 375, no. 2, p. 20, Feb. 2, 2017.

[36] K. Tsunashima and M. Sugiya, "Physical and electrochemical properties of low-viscosity phosphonium ionic liquids as potential electrolytes," *Electrochemistry Communications*, vol. 9, no. 9, pp. 2353–2358, 2007.

[37] C. Liu, Z. G. Neale, and G. Cao, "Understanding electrochemical potentials of cathode materials in rechargeable batteries," *Materials Today*, vol. 19, no. 2, pp. 109–123, 2016.

[38] L. Fransson, T. Eriksson, K. Edström, T. Gustafsson, and J. Thomas, "Influence of carbon black and binder on li-ion batteries," *Journal of Power Sources*, vol. 101, no. 1, pp. 1–9, 2001.

[39] T. Or, S. W. D. Gourley, K. Kaliyappan, A. Yu, and Z. Chen, "Recycling of mixed cathode lithium-ion batteries for electric vehicles: Current status and future outlook," *Carbon Energy*, vol. 2, no. 1, pp. 6–43, 2020.

[40] Z. Ahsan, B. Ding, Z. Cai, *et al.*, "Recent progress in capacity enhancement of LiFePO4 cathode for li-ion batteries," *Journal of Electrochemical Energy Conversion and Storage*, vol. 18, no. 1, Jun. 2020.

[41] Y. Lyu, X. Wu, K. Wang, *et al.*, "An overview on the advances of licoo2 cathodes for lithium-ion batteries," *Advanced Energy Materials*, vol. 11, no. 2, p. 2 000 982, 2021.

[42] C. Tian, F. Lin, and M. M. Doeff, "Electrochemical characteristics of layered transition metal oxide cathode materials for lithium ion batteries: Surface, bulk behavior, and thermal properties," *Accounts of Chemical Research*, vol. 51, no. 1, pp. 89–96, 2018.

[43] X. Qi, B. Blizanac, A. DuPasquier, *et al.*, "Investigation of pf6- and tfsi- anion intercalation into graphitized carbon blacks and its influence on high voltage lithium ion batteries," *Physical Chemistry Chemical Physics*, vol. 16, pp. 25 306–25 313, 46 Nov. 2014.

[44] M. E. Spahr, D. Goers, A. Leone, S. Stallone, and E. Grivei, "Development of carbon conductive additives for advanced lithium ion batteries," *Journal of Power Sources*, vol. 196, no. 7, pp. 3404–3413, 2011.

[45] B. J. Landi, M. J. Ganter, C. D. Cress, R. A. DiLeo, and R. P. Raffaelle, "Carbon nanotubes for lithium ion batteries," *Energy Environ. Sci.*, vol. 2, pp. 638–654, 6 2009.

[46] C. Qi, X. Ma, G. Ning, *et al.*, "Aqueous slurry of s-doped carbon nanotubes as conductive additive for lithium ion batteries," *Carbon*, vol. 92, pp. 245–253, 2015, Carbon Materials in Energy Storage and Conversion, Dedicated to the 5th Anniversary of the School of Energy at Soochow University.

[47] R. Sliz, J. Valikangas, H. Silva Santos, *et al.*, "Suitable cathode nmp replacement for efficient sustainable printed li-ion batteries," *ACS Applied Energy Materials*, vol. 5, no. 4, pp. 4047–4058, 2022.

[48] R. Jagau, F. Huttner, J. K. Mayer, *et al.*, "Influence of different alginate and carboxymethyl cellulose binders on moisture content, electrode structure, and

electrochemical properties of graphite-based anodes for lithium-ion batteries," *Energy Technology*, vol. n/a, no. n/a, p. 2 200 871,

[49] R. Wang, L. Feng, W. Yang, *et al.*, "Effect of different binders on the electrochemical performance of metal oxide anode for lithium-ion batteries," *Nanoscale Research Letters*, vol. 12, no. 1, p. 575, Oct. 30, 2017.

[50] C. Yin, H. Zhou, Z. Yang, and J. Li, "Synthesis and electrochemical properties of lini0.5mn1.5o4 for li-ion batteries by the metal–organic framework method," *ACS Applied Materials & Interfaces*, vol. 10, no. 16, pp. 13 625–13 634, 2018.

[51] L. Hanf, J. Henschel, M. Diehl, M. Winter, and S. Nowak, "Mn2+ or mn3+? investigating transition metal dissolution of manganese species in lithium ion battery electrolytes by capillary electrophoresis," *ELECTROPHORESIS*, vol. 41, no. 9, pp. 697–704, 2020.

[52] S. Brutti, G. Greco, P. Reale, and S. Panero, "Insights about the irreversible capacity of lini0.5mn1.5o4 cathode materials in lithium batteries," *Electrochimica Acta*, vol. 106, pp. 483–493, 2013.

[53] N. P. W. Pieczonka, Z. Liu, P. Lu, *et al.*, "Understanding transition-metal dissolution behavior in lini0.5mn1.5o4 high-voltage spinel for lithium ion batteries," *The Journal of Physical Chemistry C*, vol. 117, no. 31, pp. 15 947–15 957, 2013.

[54] D. Lu, M. Xu, L. Zhou, A. Garsuch, and B. L. Lucht, "Failure mechanism of graphite/lini0.5mn1.5o4 cells at high voltage and elevated temperature," *Journal of The Electrochemical Society*, vol. 160, no. 5, A3138, Mar. 2013.

[55] B. McENANEY, "Chapter 1 - structure and bonding in carbon materials," in *Carbon Materials for Advanced Technologies*, T. D. Burchell, Ed., Oxford: Elsevier Science Ltd, 1999, pp. 1–33, ISBN: 978-0-08-042683-9.

[56] O. Hod, "Graphite and hexagonal boron-nitride have the same interlayer distance. why?" *Journal of Chemical Theory and Computation*, vol. 8, no. 4, pp. 1360–1369, 2012.

[57] Z. Li, C. Lu, Z. Xia, Y. Zhou, and Z. Luo, "X-ray diffraction patterns of graphite and turbostratic carbon," *Carbon*, vol. 45, no. 8, pp. 1686–1695, 2007.

[58] B. Wang, B. V. Cunning, N. Y. Kim, *et al.*, "Ultrastiff, strong, and highly thermally conductive crystalline graphitic films with mixed stacking order," *Advanced Materials*, vol. 31, no. 29, p. 1 903 039, 2019.

[59] J. Asenbauer, T. Eisenmann, M. Kuenzel, A. Kazzazi, Z. Chen, and D. Bresser, "The success story of graphite as a lithium-ion anode material – fundamentals, remaining challenges, and recent developments including silicon (oxide) composites," *Sustainable Energy Fuels*, vol. 4, pp. 5387–5416, 11 2020.

[60] T. Tran and K. Kinoshita, "Lithium intercalation/deintercalation behavior of basal and edge planes of highly oriented pyrolytic graphite and graphite powder," *Journal of Electroanalytical Chemistry*, vol. 386, no. 1, pp. 221–224, 1995.

[61] H. Boehm, "Some aspects of the surface chemistry of carbon blacks and other carbons," *Carbon*, vol. 32, no. 5, pp. 759–769, 1994.

[62] S. Ko, Y. Yamada, and A. Yamada, "An overlooked issue for high-voltage li-ion batteries: Suppressing the intercalation of anions into conductive carbon," *Joule*, vol. 5, pp. 998–1009, 4 Apr. 2021.

[63] T. Placke, S. Rothermel, O. Fromm, *et al.*, "Influence of graphite characteristics on the electrochemical intercalation of bis(trifluoromethanesulfonyl) imide anions into a graphite-based cathode," *Journal of The Electrochemical Society*, vol. 160, A1979–A1991, 11 2013.

[64] K. Beltrop, P. Meister, S. Klein, *et al.*, "Does size really matter? new insights into the intercalation behavior of anions into a graphite-based positive electrode for dual-ion batteries," *Electrochimica Acta*, vol. 209, pp. 44–55, 2016.

[65] J. A. Read, "In-situ studies on the electrochemical intercalation of hexafluorophosphate anion in graphite with selective cointercalation of solvent," *The Journal of Physical Chemistry C*, vol. 119, no. 16, pp. 8438–8446, 2015.

[66] T. Placke, G. Schmuelling, R. Kloepsch, *et al.*, "In situ x-ray diffraction studies of cation and anion intercalation into graphitic carbons for electrochemical energy storage applications," *Zeitschrift für anorganische und allgemeine Chemie*, vol. 640, pp. 1996–2006, 10 Aug. 2014.

[67] A. Kotronia, H. D. Asfaw, C.-W. Tai, M. Hahlin, D. Brandell, and K. Edström, "Nature of the cathode–electrolyte interface in highly concentrated electrolytes used in graphite dual-ion batteries," *ACS Applied Materials & Interfaces*, vol. 13, no. 3, pp. 3867–3880, 2021.

[68] R. Younesi, A. S. Christiansen, R. Scipioni, *et al.*, "Analysis of the interphase on carbon black formed in high voltage batteries," *Journal of The Electrochemical Society*, vol. 162, no. 7, A1289, Apr. 2015.

[69] L. Yang, B. Ravdel, and B. L. Lucht, "Electrolyte reactions with the surface of high voltage lini0.5mn1.5o4 cathodes for lithium-ion batteries," *Electrochemical and Solid-State Letters*, vol. 13, no. 8, A95, May 2010.

[70] H. J. Lee, Z. Brown, Y. Zhao, *et al.*, "Ordered lini0.5mn1.5o4 cathode in bis(fluorosulfonyl)imide-based ionic liquid electrolyte: Importance of the cathode–electrolyte interphase," *Chemistry of Materials*, vol. 33, no. 4, pp. 1238–1248, 2021.

[71] K. J. Carroll, M.-C. Yang, G. M. Veith, N. J. Dudney, and Y. S. Meng, "Intrinsic surface stability in $LiMn_{2-x}Ni_xO_{4-\delta}$ (x = 0.45, 0.5) high voltage spinel materials

for lithium ion batteries," *Electrochemical and Solid-State Letters*, vol. 15, no. 5, A72, Mar. 2012.

[72] N. Elgrishi, K. J. Rountree, B. D. McCarthy, E. S. Rountree, T. T. Eisenhart, and J. L. Dempsey, "A Practical Beginner's Guide to Cyclic Voltammetry," *Journal of Chemical Education*, vol. 95, no. 2, pp. 197–206, Feb. 2018.

[73] J. Hjelen, *Scanning elektron-mikroskopi*, nob, Trondheim, 1989.

[74] A. Garratt-Reed, *Energy-dispersive x-ray analysis in the electron microscope*, eng, Oxford, 2003.

[75] H. Khan, A. S. Yerramilli, A. D'Oliveira, T. L. Alford, D. C. Boffito, and G. S. Patience, "Experimental methods in chemical engineering: X-ray diffraction spectroscopy—xrd," *The Canadian Journal of Chemical Engineering*, vol. 98, no. 6, pp. 1255–1266, 2020.

[76] T. Ungár, "Microstructural parameters from x-ray diffraction peak broadening," *Scripta Materialia*, vol. 51, no. 8, pp. 777–781, 2004.

[77] Q. T. Ain, S. H. Haq, A. Alshammari, M. A. Al-Mutlaq, and M. N. Anjum, "The systemic effect of peg-ngo-induced oxidative stress in vivo in a rodent model," *Beilstein Journal of Nanotechnology*, vol. 10, pp. 901–911, 2019.

[78] C. O. Ayieko, R. J. Musembi, A. A. Ogacho, B. O. Aduda, B. M. Muthoka, and P. K. Jain, "Controlled texturing of aluminum sheet for solar energy applications," *Advances in Materials Physics and Chemistry*, vol. 05, pp. 458–466, 11 2015.

[79] B. C. Smith, *Fundamentals of Fourier transform infrared spectroscopy*, eng, 2nd ed. Boca Raton, Fla: CRC Press, 2011, ISBN: 9781420069297.

[80] J. J. Ojeda and M. Dittrich, "Fourier transform infrared spectroscopy for molecular analysis of microbial cells," in *Microbial Systems Biology: Methods and Protocols*, A. Navid, Ed. Totowa, NJ: Humana Press, 2012, pp. 187–211.

[81] M. Mohamed, J. Jaafar, A. Ismail, M. Othman, and M. Rahman, "Chapter 1 - Fourier Transform Infrared (FTIR) Spectroscopy," in *Membrane Characterization*, N. Hilal, A. F. Ismail, T. Matsuura, and D. Oatley-Radcliffe, Eds., Elsevier, 2017, pp. 3–29, ISBN: 978-0-444-63776-5.

[82] J. E. Katon and M. D. Cohen, "The Vibrational Spectra and Structure of Dimethyl Carbonate and its Conformational Behavior," *Canadian Journal of Chemistry*, vol. 53, no. 9, pp. 1378–1386, 1975.

[83] W. Cai, R. Chen, Y. Yang, M. Yi, and L. Xiang, "Removal of so42- from li2co3 by recrystallization in na2co3 solution," *Crystals*, vol. 8, no. 1, 2018.

[84] D. Aurbach, B. Markovsky, A. Shechter, Y. Ein-Eli, and H. Cohen, "A Comparative Study of Synthetic Graphite and Li Electrodes in Electrolyte Solutions

Based on Ethylene Carbonate-Dimethyl Carbonate Mixtures," *Journal of The Electrochemical Society*, vol. 143, no. 12, p. 3809, 1996.

[85] G. M. A. Girard, *Investigation of phosphonium bis(fluorosulfonyl)imide-based ionic liquid electrolytes for lithium batteries*, PhD thesis, Deakin University, 2016.

[86] J. Huang and A. F. Hollenkamp, "Thermal Behavior of Ionic Liquids Containing the FSI Anion and the Li+ Cation," *The Journal of Physical Chemistry C*, vol. 114, no. 49, pp. 21 840–21 847, 2010.

[87] M. S. Malmer, Master's thesis written spring 2023 at NTNU, 2023.

[88] T. Placke, O. Fromm, S. F. Lux, *et al.*, "Reversible intercalation of bis(trifluoromethanesulfonyl)imide anions from an ionic liquid electrolyte into graphite for high performance dual-ion cells," *Journal of The Electrochemical Society*, vol. 159, no. 11, A1755, Aug. 2012.

[89] J. M. Huesker, M. Winter, and T. Placke, "Dilatometric study of the electrochemical intercalation of bis(trifluoromethanesulfonyl) imide and hexafluorophosphate anions into carbon-based positive electrodes," *ECS Transactions*, vol. 69, no. 22, p. 9, Dec. 2015.

[90] K. Beltrop, X. Qi, T. Hering, S. Röser, M. Winter, and T. Placke, "Enabling bis(fluoro-sulfonyl)imide-based ionic liquid electrolytes for application in dual-ion batteries," *Journal of Power Sources*, vol. 373, pp. 193–202, Jan. 2018.

[91] T. Rönnhult, B. Brox, and G. Fritze, "The influence of surface topography on the x-ray intensity in electron microprobe analysis (eds/wds)," *Scanning*, vol. 9, no. 2, pp. 81–87, 1987.

[92] G. M. A. Girard, M. Hilder, H. Zhu, *et al.*, "Electrochemical and physicochemical properties of small phosphonium cation ionic liquid electrolytes with high lithium salt content," *Phys. Chem. Chem. Phys.*, vol. 17, pp. 8706–8713, 14 2015.

[93] E. R. Østli, A. Mathew, J. R. Tolchard, *et al.*, "Stabilizing the cathode interphase of lnmo using an ionic-liquid based electrolyte," *Batteries & Supercaps*, vol. n/a, no. n/a, e202300085,

[94] J. Entwistle, R. Ge, K. Pardikar, R. Smith, and D. Cumming, "Carbon binder domain networks and electrical conductivity in lithium-ion battery electrodes: A critical review," *Renewable and Sustainable Energy Reviews*, vol. 166, p. 112 624, 2022.

Appendices

Appendix A

Additional slurry information

Table A.1: The slurry compositions. Slurries marked with * became the casts used in the experiments.

Cast	LNMO [g]	Carbon [g]	PVDF [g]	NMP [g]	CMC [g]	Water [g]
LNMO, C65*	0.5001	0.0273	0.0288	1.1346	-	-
LNMO, SFG6L*	0.5004	0.0278	0.0280	0.5311	-	-
Graphite	-	0.5003	0.0563	1.1227	-	-
Graphite*	-	0.3004	0.0338	0.9057	-	-
Graphite	-	0.4993	-	-	0.0557	1.8502
Graphite	-	0.5000	-	-	0.0555	1.2296
Graphite*	-	0.5007	-	-	0.0570	1.4041
Carbon black	-	0.3006	-	-	0.0337	2.2672
Carbon black*	-	0.2008	-	-	0.0353	1.4508

Multiple slurries were made, but not all successfully made cathode casts. The chosen ones were the ones that had the best viscosity, making casts with relatively even thickness.

Appendix B

Onset potentials for individual cells

Table B.1: Onset potentials for oxidation reactions. Values are given for individual cells, and for the G:0.79m cells with CMC as binder, onset potential for the 2nd cycle is also given.

	Onset potential [V]	
Cell	1st cycle	2nd cycle
G:0.79m (PVDF)	4.53	
G:0.79m (PVDF)	4.53	
G:0.79m (CMC)	4.58	4.55
G:0.79m (CMC)	4.58	4.55
G:0.79m (CMC)	4.59	4.55
G:3m	4.58	
G:3m	4.63	
G:3m	4.64	
CB:0.79m	4.62	
CB:0.79m	4.58	
CB:0.79m	4.58	
CB:3m	4.71	
CB:3m	4.60	
CB:3m	4.63	
CC:0.79m	4.48	
CC:0.79m	4.52	
CC:0.79m	4.42	
CC:3m	4.53	
CC:3m	4.54	
CC:3m	4.48	

Appendix C

Additional EDS information

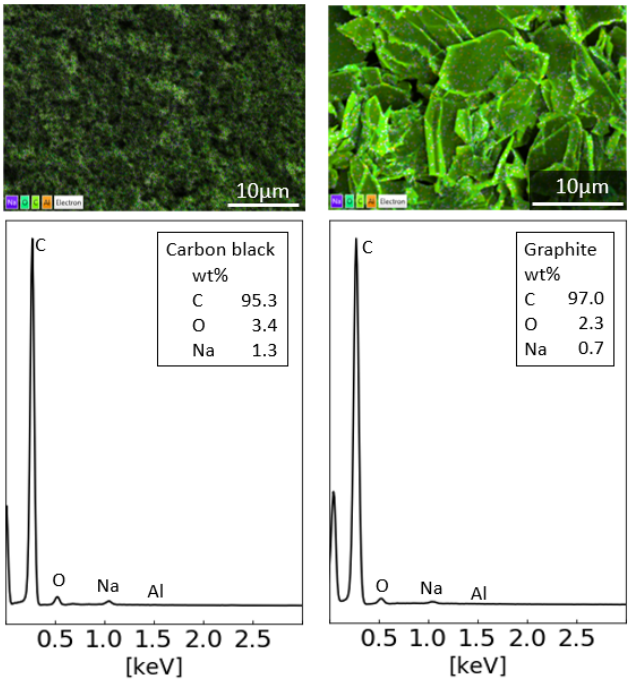

Figure C.1: Layered EDS images presenting the findings of all elements, carbon, oxygen, sodium and aluminium, together with the EDS spectra.

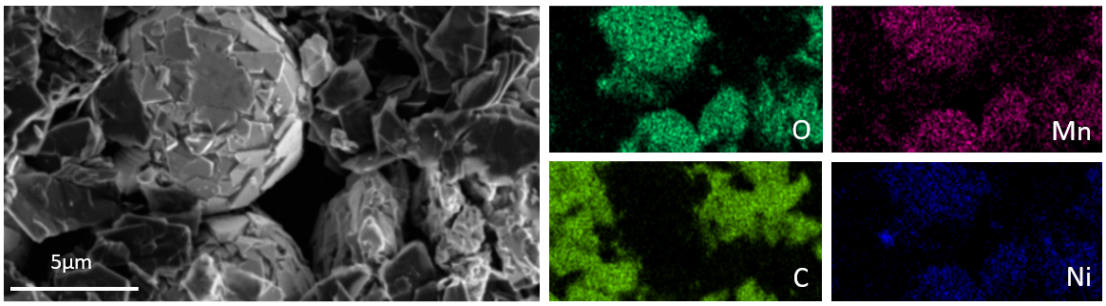

Figure C.2: EDS maps for pristine LNMO cathode with graphite as conductive additive.

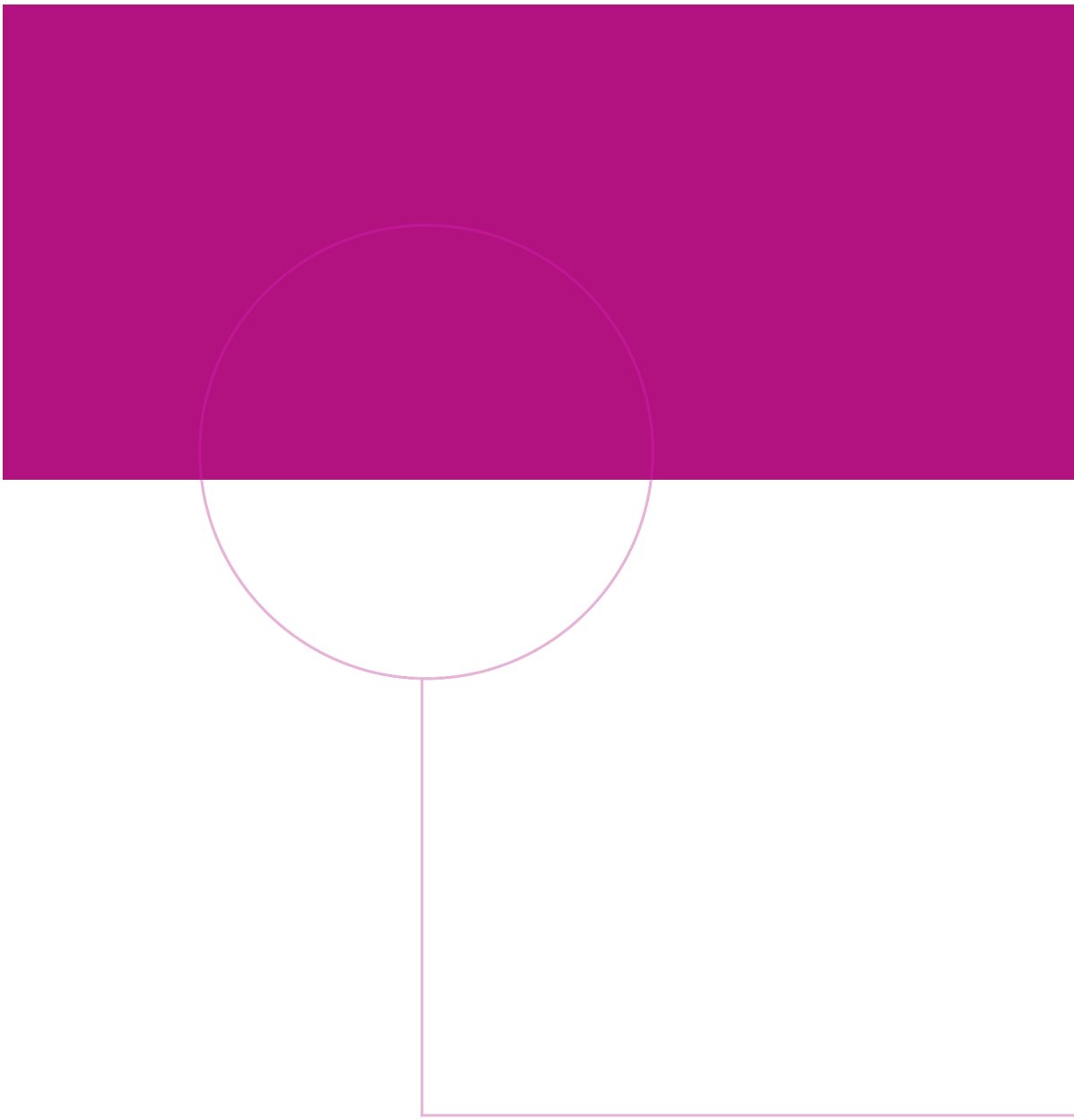

NTNU

Norwegian University of
Science and Technology